UNIVERSITY OF COPENHAGEN

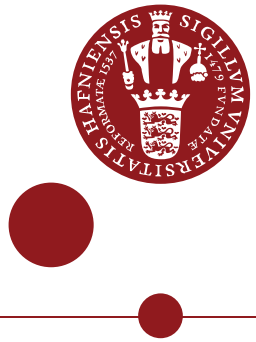

MSc in Quantum Physics

Characterization of quantum state of light emitted by quantum emitter

Georgia Anyfantaki

Supervised by Dr Alexey Tiranov and Prof Peter Lodahl

May 2022

Georgia Anyfantaki

Characterization of quantum state of light emitted by quantum emitter

MSc in Quantum Physics, May 2022

Supervisors: Dr Alexey Tiranov and Prof Peter Lodahl

University of Copenhagen

Niels Bohr Institute

Masters Degree in Quantum Physics

Blegdamsvej 17

2100 Copenhagen East

Abstract

Efficient and robust light-matter interactions schemes are essential for the advancement of quantum information protocols, quantum communication and quantum metrology. For this work, an unbalanced Mach-Zehnder interferometer was constructed, in order to investigate the quantum state of light that interacted with a solid-state self-assembled quantum dot embedded in a 1D photonic crystal waveguide. After stabilization and phase locking of the MZI, the visibility was above 99%. The UMZI was then used to probe the interference of a resonant light field that interacted with the quantum dot as a function of excitation power. It was demonstrated that the visibility in the reflected mode decreased as the power increased, whereas in the transmitted mode, the visibility firstly decreased, but then increased again. The nonlinear nature of the interaction gave rise to entangled states in the transmitted mode. To investigate that, a second identical UMZI was used to perform coincidence measurements as a function of the interferometer's phase and the excitation power. The visibility of the coincidence count rate can yield insight as to whether the state would violate the CHSH inequality and it was found that it would, under some assumptions. Theoretical fits were performed for all the measurements, setting the building blocks for the development of a theoretical model.

Acknowledgements

This thesis contains the work that I have conducted in the HyQ lab of the Quantum Photonics group in Niels Bohr institute. Firstly, I want to thank Alexey Tiranov for introducing me to this project and for helping me at every step of the process, with labwork, data analysis and theory. I would like to thank Shikai Liu for helping me in the lab and for all the enlightening discussions we've had. I very much enjoyed working in the HyQ lab and for that I have to thank all the people there for creating such an atmosphere, Vasso, Sjaak, Hania and Nils. I am extremely grateful for the help I received and happy to have collaborated with everyone. Also, I would like to help professor Peter Lodahl for giving me this opportunity and for having created such a welcoming group. Finally, I want to thank my friends, Daniel and Love, for keeping the spirits high.

Contents

1 Introduction

Quantum states of light find numerous applications, such as in precision metrology [18], [24] and in quantum information processing [10], [16]. Manipulation of well-defined quantum states of light and being able to perform operations on them are the two fundamental building blocks of quantum information. Therefore, in the past years there has been an increasing necessity in having highly efficient and coherent light-matter interactions. To that end, nanophotonic crystal waveguides have been employed, coupled with solid-state emitters, specifically solid-state quantum dots. These systems have seen much use in the recent years and have drawn a lot of focus within the field of quantum nonlinear optics, because of some very important properties such as

- light-matter coupling efficiency is almost unity [1]
- strong optical transitions, almost exclusive zero phonon line emission and ease of integration into optoelectronic devices [20], [23], [2], [3]
- single-photon non-linear interactions [9], [7]

In this thesis, we are interested in the resulting quantum state of light scattered by a solid-state quantum dot and interfered with the spontaneously emitted photons, especially the coherent properties of the single photon component transmitted and reflected from the waveguide as well as the time-energy entanglement of the two-photon component are analyzed in detail. To accomplish this, the phase stabilized unbalanced Mach-Zehnder interferometer built during this thesis was used.

1.1 Motivation

Specific focus has been given to the characterization and manipulation of the quantum state of light scattered by quantum dots embedded in photonic crystal waveguides, referred to in the bibliography as *resonance fluorescence*. Light scattered by an ideal two-level emitter is always antibunched under perfect detection conditions, but the underlying physical mechanism is dependent on the driving regime, whether it is weak or strong [8].

In the weak driving regime, often termed as Rayleigh driving regime, the light shows antibunching that is owed to the interference of the coherent and incoherent component of the emitted light field. According to the works of [19], the reflected light showed antibunched photon statistics and it was demonstrated that the electric field variance was quadrature squeezed simultaneously; a surprising effect as single photons do not have a well-defined phase. This form of squeezing is attributed to the existence of coherences between the zero and one photon component of the emitted light field. There is no classical analogue to this phenomenon and it is a fully quantum demonstration of the wave-particle nature of light. The studies led by [8] and [17] further investigated this, showing that the emitted light field can be decomposed into a coherent and an incoherent component; the first one inherits the statistics of the laser and the latter inherits the statistics of the two-level system. The interference between these two components is the reason for the antibunched photon statistics in the reflected component, resulting in quadrature squeezing [8]. This is further corroborated by [17], whereby it was shown that by varying the fraction of the coherent versus incoherent component by filtering techniques, the photon statistics changed from antibunched to bunched. In the strong driving regime, on the other hand, antibunching is a consequence of the sub-Poissonian photon statistics of the spontaneously emitted single photons by the saturated quantum emitter.

On the other hand, the transmitted component of the light field shows photon bunching in the weak driving regime and the strong driving regime the coherent state describing the laser dominates. In the weak driving regime, a laser beam can be approximated by a weak coherent state

$$|\psi\rangle = a_0 |0\rangle + a_1 |1\rangle + a_2 |2\rangle \tag{1.1}$$

The photon statistics of the reflected component show antibunching, whereas for the transmitted they show bunching. Therefore, the nonlinear nature of the light field's interaction with the quantum dot results in it reflecting the $|0\rangle, |1\rangle$ components and transmitting the $|2\rangle$. Another consequence of the nonlinearity of the emitter-light interaction is the time-energy entanglement of the emitted two-photon states. The coherent process of converting the two photon state of the driving field to the two photon state of the emitted field conserves energy and thus, ensures energy-time entanglement. Time-energy entanglement is highly employed in the field of Quantum communication [15].

1.2 Description of this thesis

In Chapter 2, the theory of light-matter interactions is presented. In more detail, the two-level system and field operators are presented, followed by a description of their dynamics in Schrödinger and Heisenberg pictures. Afterwards, we consider the case of open quantum systems using *System-reservoir theory*, we develop their dynamics using the Master equation and Langevin equations and noise operators and consider how the properties of the smaller quantum system are affected. Finally, we use the previous tools to describe to derive the reduced density matrix of the emitter in the steady state and the model of *resonant transmission* through a waveguide.

In Chapter 3, the first and second order coherence functions are presented for the modes coupled to a chiral and a non-chiral waveguide. A reminder about the interference pattern and the visibility is given and how the visibility relates to the first order coherence function. Finally, the time-energy entanglement of the two-photon state in the transmitted mode is introduced.

In Chapter 4, the constructed interferometer is presented in detail. There, a detailed description of it can be found as well as of the process of stabilization

and phase locking. Lastly, a few words of how the UMZI was operated for our experiments thus far.

In Chapter 5, the experiments that were conducted can be found with the experimental results. The first experiment describes how the emitter was excited in order to characterize it and witness the single-photon nonlinearity that gives rise to all sorts of interesting phenomena. Secondly, using the UMZI, the visibility of light in the reflected and transmitted modes was explored as a function of laser excitation power. Finally, the two-photon state of the transmitted mode was guided into two identical UMZIs to probe the entangled two-photon state of the transmitted mode using the Franson interferometer.

Lastly, in Chapter 6, a brief summary is given to remind the reader of the experiments and their results. Following the summary, a few words regarding the experimental results, deviations from theory, imperfections in the setups and in generally, conclusions can be found and possible improvements or suggestions for the future.

2

Theoretical Background. Light interacting with TLS

The aim of this chapter is to provide the necessary theoretical background and formalism relevant to a light field interacting with a two-level system. The system's dynamics will be presented in the form of the master equation. Afterwards, the model for resonant fluorescence and transmission in a waveguide will be described.

2.1 Quantum emitter

The quantum emitter of interest in this work is a solid-state quantum dot. A quantum dot is an artificial two-level system, therefore the dynamics of interest are those of a two-level system. The two levels of the emitter are denoted by $|g\rangle$, ground state, and by $|e\rangle$, excited state. The atomic raising operator is expressed as $\hat{\sigma}_{ge} = |e\rangle\langle g|$ and the lowering operator as $\hat{\sigma}_{eg} = |g\rangle\langle e|$.

The dynamics of the emitter can be expressed using the Schrödinger or the Heisenberg picture, depending on whether we are interested in the time evolution of the atomic operators (Heisenberg picture) or the density matrix (Schrödinger picture).

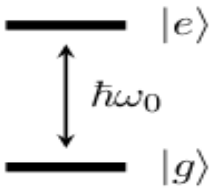

Figure 2.1: Energy schematic of a two-level system. We denote by $|g\rangle$ the ground state and by $|e\rangle$ the excited state. The energy of the transition is given by $\Delta E = \hbar\omega_0$. Figure adapted from [21].

2.2 Light field

The quantized light field is described as a harmonic oscillator if we consider a monochromatic field or a sum of harmonic oscillators for a field containing a sum of frequencies, with the most realistic case being the latter. For the purposes of this work the monochromatic field is an adequate approximation. We describe the light field using the bosonic creation and annihilation operators, $\hat{a}^\dagger$ and $\hat{a}$, which act on a number state $|n\rangle$ as

$$\hat{a}^\dagger |n\rangle = \sqrt{n+1}\,|n+1\rangle\,, \tag{2.1}$$

$$\hat{a}\,|n\rangle = \sqrt{n}\,|n-1\rangle\,, \tag{2.2}$$

The dynamics of the electric field are given by the Heisenberg equation of motion

$$\frac{d\hat{a}}{dt} = \frac{i}{\hbar}[\hat{H}, \hat{a}], \tag{2.3}$$

where $\hat{H}$ is the Hamiltonian of the system.

2.3 System-reservoir interactions

There are two ways to time-evolve a closed system in quantum mechanics, the Heisenberg and the Schrödinger picture. Similarly, when a small quantum system is coupled to a larger system, called a *bath* or *reservoir*, there are two ways to study the dynamics of the system-reservoir interactions. The first one is based on the Schrödinger picture and leads to the master equation and the second one is based on the Heisenberg equation of motion and leads to the existence of quantum noise operators by solving the Langevin equations. Relevant to this work are both pictures and thus a brief description of both shall be given.

A quantum emitter in a photonic waveguide is in reality coupled to a continuum of optical modes; the optical modes of the waveguide and the loss into the environment. The generic Hamiltonian of any two-level system coupled into a reservoir is given by equation 2.4

$$\hat{H}_{total} = -\frac{1}{2}\hbar\omega\hat{\sigma}_z + \sum_j \hbar\Omega_j \hat{b}_j^\dagger \hat{b}_j + \sum_j \hbar(g_j\hat{\sigma}_+\hat{b}_j + g_j^\star\hat{\sigma}_-\hat{b}_j^\dagger), \tag{2.4}$$

where the first term expresses the energy of the emitter, with $\hbar\omega$ being the energy separation of the two states, the second term expresses the reservoir with energy $\hbar\Omega_j$ and $\hat{b}_j^\dagger$, $\hat{b}_j$ the creation and annihilation operators, respectively, of the j-th mode and the third term is the interaction term, which expresses the coupling between the two-level system and the reservoir of modes, with g_j being the coupling strength of the j-th mode and the emitter. Note that the rotating wave approximation has been applied in the interaction term.

The Hamiltonian can therefore be written as the sum of two terms, H_0, which entails the Hermitian part of the Hamiltonian and H_{int}, the non-Hermitian term, expressing the coupling with the reservoir leading to irreversible damping and decoherence.

2.3.1 Langevin equations

In the Langevin formalism, the reservoir operators can be interpreted in the same way as Langevin forces in classical statistical mechanics. The time-evolution of any system operator $\hat{A}$, can be written as

$$\frac{d\hat{A}}{dt} = -\frac{\gamma}{2}\hat{A} + \hat{F}(t). \tag{2.5}$$

Equation 2.5 is called the quantum Langevin equation and $\hat{F}(t)$ the quantum noise operator, containing only reservoir operators and the coupling strength with the system. The noise operator expresses a random fluctuating force and is responsible for the fluctuations induced on the system by the reservoir and for the irreversible dissipation of energy from the system to the reservoir.

Properties of the noise operator:

- Expectation value $\left\langle \hat{F}(t) \right\rangle = 0$

- Two-time autocorrelation function $\left\langle \hat{F}(t)\hat{F}(t')\right\rangle = 0$

- Two-time correlation function $\left\langle \hat{F}(t)\hat{F}^{\dagger}(t')\right\rangle \neq 0$

The two time correlation functions of the noise operators are not equal, $\left\langle \hat{F}(t)\hat{F}^{\dagger}(t')\right\rangle \neq \left\langle \hat{F}^{\dagger}(t)\hat{F}(t')\right\rangle$ because on non-commutativity and they yield the spectral properties of the operators.

2.3.2 Master equation

The master equation yields the dynamics of the reduced density matrix of the system in the Schrödinger picture. The whole derivation will not be presented here, but rather the methodology and the assumptions made. We begin by defining the density operator of the system-reservoir

$$\hat{\rho}_{sr} = \sum_i p_i \left|\psi_i\right\rangle \left\langle\psi_i\right|, \tag{2.6}$$

The time-evolution of a density matrix in the Schrödinger picture is given by the von Neumann equation

$$\dot{\hat{\rho}}_{sr} = -\frac{i}{\hbar}\left[\hat{H}, \hat{\rho}_{sr}\right], \tag{2.7}$$

In order to derive the exact form of the master equation, we switch to the interaction picture, then integrate the von Neumann equation and then trace out the reservoir, since the dynamics of only the small quantum system are of interest. Afterwards, we make three very important assumptions:

- Separability assumption: at t = 0 the system and the reservoir are independent, meaning that $\hat{\rho}_{sr}(0) = \hat{\rho}_s(0) \otimes \hat{\rho}_r(0)$

- Born approximation: the reservoir is unaffected by the system, meaning that $\hat{\rho}_{sr}(t) = \hat{\rho}_s(t)\hat{\rho}_r$ and $\dot{\hat{\rho}}_r = 0$

- Markoff approximation: the correlation time of the reservoir is infinitely short compared to all times of interest for the system

Finally, in the Schrödinger picture the master equation of a two-level system coupled to a reservoir of harmonic oscillators can be written as:

$$\dot{\hat{\rho}}_s = -\frac{i}{\hbar}\left[\hat{H}_0, \hat{\rho}_s\right] + L[\rho], \tag{2.8}$$

where the term $L[\rho]$ is called the Liouvillian or Lindblad operator and it expresses the non-Hermitian evolution of the system because of its coupling to the reservoir. It is the term that describes the dissipative and decoherence processes of the Hamiltonian.

$$L[\rho] = -\frac{1}{\hbar^2}\sum_{ij}\frac{\gamma_{ij}}{2}(\hat{\sigma}_j\hat{\sigma}_i\hat{\rho}_s + \hat{\rho}_s\hat{\sigma}_j\hat{\sigma}_i) + \frac{1}{\hbar^2}\sum_{ij}\gamma_{ij}\hat{\sigma}_i\hat{\rho}_s\hat{\sigma}_j, \tag{2.9}$$

where γ_{ij} is the rate of dissipation and/or decoherence, depending on the exact nature of the reservoir the system is coupled to.

The master equation can be used to calculate any expectation value of the system operators. Suppose $\hat{A}$ is a system operator, then its expectation value is equal to

$$\left\langle \hat{A}(t) \right\rangle = \mathrm{Tr}_s(\hat{A}\hat{\rho}_s(t)), \tag{2.10}$$

2.3.3 Pure dephasing

Suppose we have a two-level system, such as a solid-state quantum emitter, described by the following Hamiltonian (Equation 2.11)

$$\hat{H} = \hbar\omega\sigma_z + \hbar\delta\omega(t)\sigma_z, \tag{2.11}$$

The first term expresses the energy of the two-level system and the second perturbs the energy transition as a function of time, as illustrated in Figure 2.2. $\hat{H}_{deph} = \hbar\delta\omega(t)\sigma_z$ describes the mechanism of pure dephasing. By making use of the master equation we can see the Liouvillian of such a Hamiltonian:

$$L[\rho] = \gamma_{deph}\begin{pmatrix} 0 & -\rho_{eg} \\ -\rho_{ge} & 0 \end{pmatrix}, \tag{2.12}$$

The Liouvillian of Equation 2.12 demonstrates that a system under the influence of dephasing loses its coherences with rate γ_{deph}, while its populations do not change over time. In the case of solid-state quantum dots, pure dephasing can be induced by phonon inelastic scattering and is irreversible.

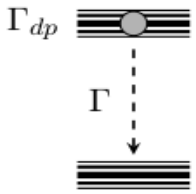

Figure 2.2: Energy schematic of a two-level system under a mechanism of dephasing. The two distinct energy levels of the TLS turn into a continuum of frequencies because of some $\delta\omega(t)$ term in the Hamiltonian. Figure adapted from [21].

2.4 Light-matter interaction I. Dynamics of the emitter

To investigate the influence of the driving laser field on the emitter in the presence of dephasing and coupling to the reservoir, a semi-classical approach is sufficient, as there is no need to quantize the electric field. The total Hamiltonian describing the system is given by equation 2.13

$$\hat{H} = -\hbar\Delta\hat{\sigma}_z + \hbar\Omega_R\hat{a}^\dagger\hat{a} - \hbar\omega(\hat{\sigma}_{eg} + \hat{\sigma}_{ge}) + \hat{H}_r + \hat{H}_{sr} + \hat{H}_{deph}, \tag{2.13}$$

Description of the Hamiltonian terms:

1. energy of the TLS in the rotating frame, meaning that we consider the detuning of the laser from the TLS $\Delta = \Omega - \omega$ with Ω and ω the laser and TLS, frequencies, respectively.

2. energy of the laser with $\Omega_R = \frac{d^* E^+}{\hbar}$ the classical Rabi frequency which indicates the strength of the coupling between the light and the TLS

3. Interaction term between TLS and laser; the field creation and annihilation operators are missing because we are taking the semi-classical approach here

4. Hamiltonian of the reservoir coupled to the TLS

5. System-reservoir interaction

6. Pure dephasing Hamiltonian of the form of equation 2.11

The derived master equation of the Hamiltonian is

$$\begin{aligned}\dot{\hat{\rho}}_s = &-\frac{i}{\hbar}\left[\hat{H}_0, \hat{\rho}_s\right] \\ &-\frac{\gamma}{2}(2\hat{\sigma}_{eg}\hat{\rho}_s\hat{\sigma}_{ge} - \hat{\sigma}_{ge}\hat{\sigma}_{eg}\hat{\rho}_s - \hat{\rho}_s\hat{\sigma}_{ge}\hat{\sigma}_{eg}) \\ &+\frac{\gamma_{deph}}{2}(\hat{\sigma}_z\hat{\rho}_s\hat{\sigma}_z - \hat{\rho}_s),\end{aligned} \tag{2.14}$$

where $\hat{H}_0 = -\hbar\Delta\hat{\sigma}_z + \hbar\Omega_R\hat{a}^\dagger\hat{a} - \hbar\omega(\hat{\sigma}_{eg} + \hat{\sigma}_{ge})$.

The first term of the master equation describes the free evolution of the two-level system and the light field. The second term describes the emitter's decay with rate γ due to the coupling with the reservoir and finally, the third term describes the dephasing of the system, causing decoherence with rate γ_{deph}.

The reduced density matrix of the emitter is given by

$$\rho_s = \begin{pmatrix} \rho_{gg} & \rho_{eg} \\ \rho_{ge} & \rho_{ee} \end{pmatrix} \tag{2.15}$$

where ρ_{gg}, ρ_{ee} are the populations of the ground and excited state of the TLS, respectively, and ρ_{ge}, ρ_{eg} are the coherences between the two states. Solving the master equation (2.14) for each of the matrix elements of Equation 2.15 above yields the following system of coupled differential equations:

$$\begin{aligned}\dot{\rho}_{gg} &= i\Omega_R(\rho_{eg} - \rho_{ge}) + \gamma\rho_{ee}, \\ \dot{\rho}_{ge} &= -(\gamma_2 + i\Delta) + i\Omega_R(\rho_{ee} - \rho_{gg}), \\ \dot{\rho}_{eg} &= -(\gamma_2 - i\Delta) - i\Omega_R(\rho_{ee} - \rho_{gg}), \\ \dot{\rho}_{ee} &= -i\Omega_R(\rho_{eg} - \rho_{ge}) - \gamma\rho_{ee},\end{aligned} \tag{2.16}$$

where we define the total decay rate $\gamma_2 = \gamma_{deph} + \frac{\gamma}{2}$.

We note that in the master equation 2.14, if we set $\gamma = \gamma_{deph} = 0$, i.e. if we consider the system TLS-laser closed with no coupling to the environment and

no dephasing mechanisms present, the result are the Rabi oscillations with no decay and no dephasing. There would be no loss of energy and the state would always be pure. On the contrary, in the presence of only dephasing, the coherences ρ_{ge}, ρ_{eg} will damp out to zero and the populations ρ_{gg}, ρ_{ee} to 1/2. The state will evolve from a pure state to a maximally mixed state. If we consider the system open, then the TLS will reach a steady state that we find by solving the coupled equations of 2.16.

2.4.1 Steady-state solution

In the presence of both dephasing and coupling to a reservoir, a two-level system excited by a cw laser will reach a steady state solution, where $\dot{\rho}_{gg} = \dot{\rho}_{ge} = \dot{\rho}_{eg} = \dot{\rho}_{ee} = 0$. In this case, the elements of the two-level system's reduced density matrix are

$$\begin{aligned}
\rho_{ee} &= \frac{2\gamma_2\Omega_R^2}{\gamma(\gamma_2^2 + \Delta^2 + 4\Omega_R^2\frac{\gamma_2}{\gamma})}, \\
\rho_{gg} &= 1 - \rho_{ee}, \\
\rho_{ge} &= -\frac{\Omega_R(\Delta + i\gamma_2)}{\gamma_2^2 + \Delta^2 + 4\Omega_R^2\frac{\gamma_2}{\gamma}}, \\
\rho_{eg} &= \rho_{ge}^{\star},
\end{aligned} \tag{2.17}$$

The lineshapes of the excited state population and of the real and imaginary part of the coherences as a function of detuning can be seen in Figure 2.3. Due to stimulated emission, the population of the excited state cannot exceed the population of the ground state as ρ_{ee}^{max} is a fixed number, determined by the values of the parameters Δ, Ω_R and γ_2. In the absence of detuning and dephasing, the excited state's population maximum value is $\rho_{ee}^{max} = 1/2$ and we can define the *mean photon field flux per emitter lifetime* as

$$\eta = 2\frac{\Omega_R^2}{\gamma^2}, \tag{2.18}$$

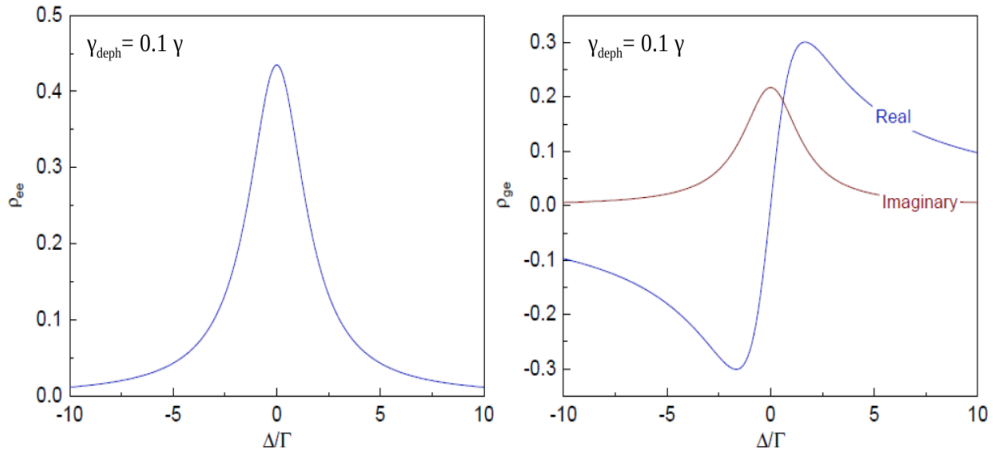

Figure 2.3: Left: Excited state population as a function of the laser detuning Δ. ρ_{ee} has a Lorrentzian lineshape with linewidth proportional to the total rate of decay γ_2 and the laser power Ω_R. Right: Real and imaginary part of the emitter's coherences. Figure taken from [12]

Similar to the photon flux, but including detuning and dephasing, we define the *emitter's saturation parameter*

$$S = \frac{4\gamma_2\Omega_R^2}{\gamma(\gamma_2^2 + \Delta^2)}. \tag{2.19}$$

We can see from Equation 2.19, that for a high dephasing rate γ_{deph} and/or detuning Δ, higher laser power is necessary to saturate the emitter. The saturation parameter is proportional to the population of the excited state and so is the emission rate (equation 2.20).

$$\gamma_{emission} = \gamma\rho_{ee} = \frac{\gamma S}{2(S+1)}. \tag{2.20}$$

The result of Equation 2.20 is important but not surprising; as the laser power increases, the rate of emission increases as well. However, at some power the emitter will get saturated and effectively become transparent to the incoming light field.

Also influenced by the driving field is the linewidth or the spectral response of the emitter. As we saw from Equation 2.17, the population of the excited state ρ_{ee} and thus the rate of spontaneous emission as a function of detuning are

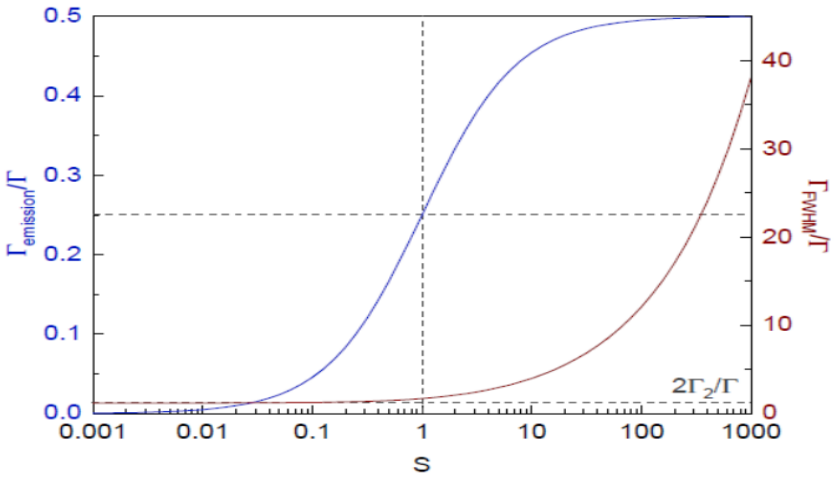

Figure 2.4: The blue curve corresponds to the rate of the spontaneous emission as a function of the saturation parameter S. The red curve demonstrates the linewidth of the spontaneous emission as a function of the saturation parameter S. It can be seen that the rate of spontaneous emission can get saturated at high powers and the linewidth can get broadened. Figure taken from [12]

described by a Lorentzian, with a power dependent linewidth. Expressed in terms of the saturation parameters, the FWHM of the emission rate is given by

$$\gamma_{FWHM} = 2\gamma_2\sqrt{S+1}. \tag{2.21}$$

We see from Equation 2.21 that in the low power limit, the linewidth of the emitter is equal to $2\gamma_2$ and in the special case of no dephasing it is γ. In this case the emitter resonance is termed *lifetime limited*. As the power increases, the linewidth increases as well. This effect is called *power broadening* and it is demonstrated in Figure 2.4

2.5 Light-matter interaction II. Dynamics of the driving field

In the previous section, we studied the dynamics of the emitter under the inflcuence of the light field, in the presence of dephasing and coupling to the environment. Now we turn our attention towards the light field itself and the objective is to investigate how the interaction with the emitter influences the light field and how the coupling to the environment and the dephasing modify the properties of the scattered and transmitted light. In this section, a semi-classical approach might conceal some of the physics as we are interested in the photons themselves, there we have to use the Hamiltonian for the quantized field, in the rotating frame and after having applied the rotating wave approximation.

$$\hat{H} = -\hbar\Delta\hat{\sigma}_z + \hbar\Omega_R\hat{a}^\dagger\hat{a} - \hbar d\hat{E} + \hat{H}_r + \hat{H}_{sr}, \tag{2.22}$$

where the terms of the Hamiltonian are:

1. Hamiltonian of the emitter in the rotating frame
2. Hamiltonian of the light field
3. Interaction Hamiltonian between quantized field and emitter
4. Hamiltonian of the reservoir
5. Interaction Hamiltonian describing the coupling between system and reservoir

In this case, we shall consider that the system TLS-light field is coupled to two distinct reservoirs, namely the waveguide and the environment. Thus, some modes couple out of the waveguide with rate γ' and other modes couple into the waveguide, with rate γ_{1D}. This distinction is necessary since the driving

field is in the waveguide itself. We define the β factor, expressing how well the light field is coupled to the waveguide, in comparison to the coupling with the environment.

$$\beta = \frac{\gamma_{1D}}{\gamma_{1D} + \gamma'}. \tag{2.23}$$

The generic electric field operator can be written as

$$\hat{E}^+(r,t) = \sum_k E_k^+(r)\hat{a}_k(t), \tag{2.24}$$

where $\hat{a}_k(t)$ is the field annihilation operator of the k-th mode.

The spontaneous emission rate into the waveguide can be calculated by Green's function

$$\gamma_{1D} = \frac{2\pi}{\hbar^2}\sum_k [\hat{d}^\star \hat{E}_k^+ \hat{E}_k^- \hat{d}]\delta(\omega_k - \omega_A), \tag{2.25}$$

where ω_k is the frequency of the k-th mode of the electric field, ω_A the frequency of the emitter's transition and $\hat{E}_k^+, \hat{E}_k^-$ are calculated at the position of the emitter, r_A.

We define the positive component of the incoming light as $\hat{E}_P^+$ and the total transmitted light as $\hat{E}^+$, as demonstrated in Figure 2.5. The fraction of the light that is scattered into the waveguide is represented by $\hat{E}_S^+$. We therefore define the transmission and reflection coefficients as

$$\begin{aligned} t &= \frac{\left\langle \hat{E}^+ \right\rangle}{\left\langle \hat{E}_P^+ \right\rangle}, \\ r &= \frac{\left\langle \hat{E}_S^+ \right\rangle}{\left\langle \hat{E}_P^+ \right\rangle}. \end{aligned} \tag{2.26}$$

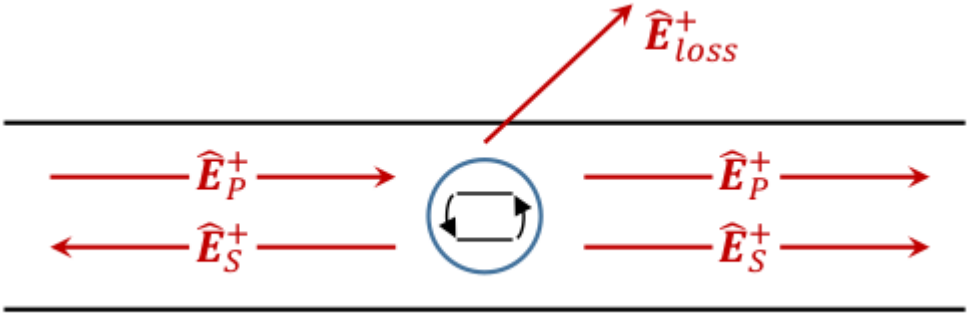

Figure 2.5: Electric field components scattered, reflected and transmitted in and out of the waveguide by the quantum emitter.

We aim to see the signature of the emitter in the transmitted and reflected component, so we need to express the field operators in terms of the emitter coherence operators. With the use of the Heisenberg-Langevin equation of motion we derive the evolution of the field operator $\hat{a}_k$

$$\frac{d\hat{a}_k(t)}{dt} = -i\omega_k \hat{a}_k(t) + \frac{i}{\hbar} \hat{d}\hat{E}_k^-(r_A)\sigma_{eg}(t), \tag{2.27}$$

Afterwards, we formally integrate the above equation from t_0 to t

$$\begin{aligned} \hat{a}_k(t) &= \hat{a}_k(t_0)e^{-i\omega_k(t-t_0)} + \frac{i}{\hbar}\hat{d}E_k^-(r_A)\int_{t_0}^{t} dt'\sigma_{eg}(t)e^{-i\omega_k(t'-t_0)} \\ &= \hat{a}_{free}(t) + \hat{a}_{scattered}(t), \end{aligned} \tag{2.28}$$

The first term of equation 2.28 describes the part of electric field that evolves without interacting with the emitter, while the second term corresponds to the electric field component that is due to the interaction with the emitter. This interaction is represented by σ_{eg} and it can represent an actual decay from the excited to the ground state or a scattering event. We insert $\hat{a}_k(t)$ of Equation 2.28 into Equation 2.24 and we derive the expression for the positive component of the electric field

$$\begin{aligned}\hat{E}^{+}(r,t) &= \sum_k (E_k^{+}(r)\hat{a}_k(t_0)e^{-i\omega_k(t-t_0)} + \frac{i}{\hbar}\hat{d}E_k^{-}(r_A)\int_{t_0}^{t} dt'\sigma_{eg}(t)e^{-i\omega_k(t'-t_0)}) \\ &= \hat{E}_{free}(t) + \sum_k \hat{d}E_k^{+}(r)E_k^{-}(r_A)\int_{t_0}^{t} dt'\sigma_{eg}(t)e^{-i\omega_k(t'-t_0)} \\ &= \hat{E}_{free}(t) + \hat{E}_{scattered}(t).\end{aligned} \tag{2.29}$$

Similarly to $\hat{a}_k(t)$ of Equation 2.28, we see that the first term corresponds to the evolution of the electric field component that did not interact with the emitter, while the second term yields the time evolution of the electric field that was scattered by the emitter at position $r = r_A$.

We now introduce the slowly varying operator $\hat{S}_{eg}(t) = \hat{\sigma}_{eg}(t)e^{i\omega_A t}$. We can use the approximations presented in the previous sections and derive the scattered component of the electric field

$$\hat{E}_S^{+}(r,t) = i\frac{\pi}{\hbar}\delta(\omega_k - \omega_A)\hat{S}_{eg}(t)\sum_k E_k^{+}(r)E_k^{-}(r_A)d, \tag{2.30}$$

We want to express the scattered field in terms of the incident field, so we multiply and divide by $d^{\star}E_P^{+}(r_A,t) = \hbar\hat{\Omega_R}$

$$\begin{aligned}\hat{E}_S^{+}(r,t) &= i\frac{\pi}{\hbar}\frac{[\sum_k d^{\star}E_k^{+}(r)E_k^{-}(r_A)d]}{d^{\star}E_P^{+}(r_A,t)}E_P^{+}(r_A,t)\delta(\omega_k-\omega_A)\hat{S}_{eg}(t) \\ &= i\frac{\pi}{\hbar^2\hat{\Omega_R}}[\sum_k d^{\star}E_k^{+}(r)E_k^{-}(r_A)d]\delta(\omega_k-\omega_A)E_P^{+}(r_A)\hat{S}_{eg}(t).\end{aligned} \tag{2.31}$$

The equation written above is quite similar to Fermi's Golden rule expression of the spontaneous emission rate, with the sole difference that instead of having $E_k^{-}(r)$, we have $E_k^{-}(r_A)$. Therefore, we need to express how the field propagates from the position of scattering, r_A, to a generic position r in the one-dimensional waveguide. A photon that propagates in such a medium will

simply gain a phase due to propagation that depends on the optical distance from the point of scattering, such that

$$E_k^+(r) = e^{ik_P|r-r_A|}E_k^+(r_A), \tag{2.32}$$

where k_P is the waveguide's propagation constant. Finally, the expression for the scattered field is

$$\hat{E}_S^+(r,t) = i\frac{\beta\gamma}{2\hat{\Omega}_R}E_P^+(r,t)\hat{S}_{eg}(t). \tag{2.33}$$

As we can see from Equation 2.33, the scattered component of the electric field is proportional to the coupling to the waveguide, β factor, the incident field and the coherence operator $\hat{S}_{eg}(t)$, but decreases with the Rabi frequency operator $\hat{\Omega}_R$. Another important thing to note is that the interaction with the emitter induced a phase shift of $\pi/2$ on the scattered field.

We now recall the form of the transmission and reflection coefficients (equation 2.26); their corresponding observables are $T = |t|^2$ and $R = |r|^2$. As such, the expression for the intensity of the transmitted and reflected components of the electric field yields

$$R = \frac{\beta^2\gamma^2}{4\hat{\Omega}_R^2}\left\langle \hat{S}_{ge}(t)\hat{S}_{eg}(t)\right\rangle, \tag{2.34}$$

$$T = 1 + i\frac{\beta\gamma}{2\hat{\Omega}_R}(\left\langle \hat{S}_{eg}(t)\right\rangle - \left\langle \hat{S}_{ge}(t)\right\rangle) + (\frac{\beta\gamma}{2\hat{\Omega}_R})^2\left\langle \hat{S}_{ge}(t)\hat{S}_{eg}(t)\right\rangle. \tag{2.35}$$

We see from equation 2.35, that the intensity of the transmitted light is comprised of three different terms that correspond to three different processes. The first term, 1, is due to the field that is transmitted through the waveguide without interacting with the emitter. The second term, proportional to $\left\langle \hat{S}_{eg}(t)\right\rangle - \left\langle \hat{S}_{ge}(t)\right\rangle = 2iIm(\rho_{eg})$, describes the photons that are scattered off the emitter without being absorbed by it. This term is referred to as the

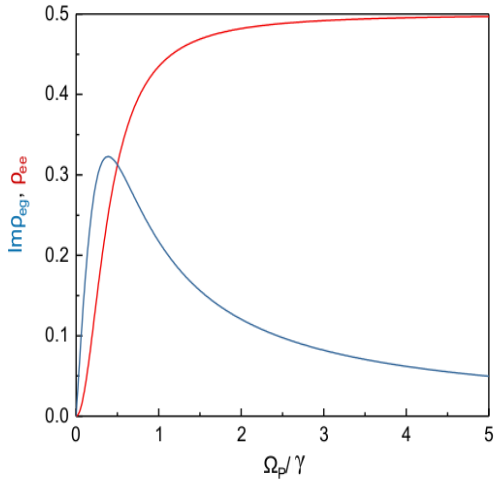

Figure 2.6: Matrix elements of emitter's the density matrix that influence the transmitted field as a function of excitation power. As we can see, at low powers, the coherent component is dominant, while as the power increases, so does the infuence of the incoherent component. Figure adapted from [12]

coherent term as in the steady state it is dependent on the coherence ρ_{eg} of the TLS. Notice that this term is multiplied by i, meaning that the photons that are scattered by the emitter without being absorbed by it are scattered with a $\pi/2$ phase difference and thus they interfere destructively with the incident light field. Finally, the last term is known as the incoherent term and it corresponds to the photons that the TLS emits as it decays, after having absorbed a photon from the incident field. This term is proportional to the population of the excited state $\left\langle \hat{S}_{ge}(t)\hat{S}_{eg}(t)\right\rangle = \left\langle \hat{S}_{ee}\right\rangle = \rho_{ee}$.

At low excitation power, the coherent component dominates while as the power increases the incoherent component takes over, as it is proportional to the population of the excited state (Figure 2.6).

We can use the steady-state solutions of the density matrix of the previous section to derive expressions for the transmitted, reflected and scattered out of the waveguide intensities of the electric field.

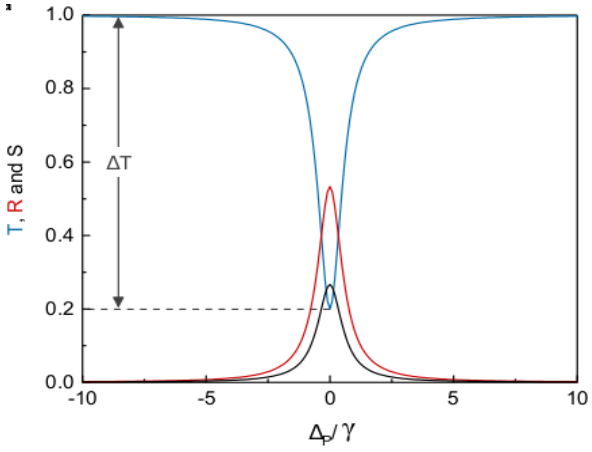

Figure 2.7: Transmitted, reflected and scattered components as a function of detuning per limit ($\Omega_R - > 0$), for $\beta = 0.8$ and $\gamma_{deph} = 0.1\gamma$. Figure adapted from [12]

$$
\begin{aligned}
T &= 1 - \frac{\beta\gamma\gamma_2(2-\beta)}{2(\gamma_2^2 + \Delta^2 + 4\Omega_R^2\frac{\gamma_2}{\gamma})}, \\
R &= \frac{\beta^2\gamma\gamma_2}{2(\gamma_2^2 + \Delta^2 + 4\Omega_R^2\frac{\gamma_2}{\gamma})}, \\
S &= \frac{\beta\gamma\gamma_2(1-\beta)}{\gamma_2^2 + \Delta^2 + 4\Omega_R^2\frac{\gamma_2}{\gamma}},
\end{aligned}
\tag{2.36}
$$

The intensities of the transmitted and reflected fields (given by equation 2.36) are plotted against the detuning per emitter lifetime Δ/γ in Figure 2.7 in the low excitation power limit ($\Omega_R - > 0$), for $\beta = 0.8$ and $\gamma_{deph} = 0.1\gamma$. On resonance, most of the photons are reflected in and out of the waveguide. The ratio of how many photons are scattered into the waveguide in relation to out of the waveguide is proportional to the β factor and for good coupling such as $\beta = 0.8$, we see that most of the photons are scattered into the waveguide. On the contrary, close to resonance we see a transmission dip, which we call *coherent extinction* since it is due to the interference of the coherently scattered photons with the emitted photons. The interference is owed to the fact that the scattered photons have undergone a phase shift of $\pi/2$ due to interaction with the emitter.

Finally, we plot the coherent extinction as a function of excitation power (Figure 2.8) and notice the nonlinear behavior. In the low-power limit, almost no light is transmitted while for higher powers the emitter is saturated and thus all

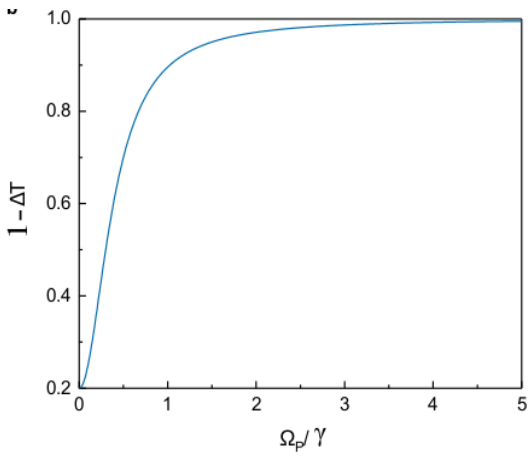

Figure 2.8: Transmission as a function of average photon number for $\Delta = 0$, $\beta = 0.8$ and $\gamma_{deph} = 0.1\gamma$. Figure adapted from [12]

of the light can be transmitted. This is referred to as *single photon nonlinearity* of the quantum dot, stating that when the field can be approximated with single photons most of them are reflected by the emitter. On the other hand, at higher powers, the incoherent contribution increases as the population of the excited state increases and photons are emitted in both directions, rather than being mostly reflected as in the low-power limit. Additionally, we observe that the emitter is saturated, meaning that during one emitter lifetime, more than one photons pass through the TLS without interacting with it.

2.5.1 Decoherence mechanisms and their influence on transmission

In order to connect the theoretical foundation built in this chapter and explain the deviations from it that shall be seen in Chapter 5, we need to understand how the various emitter parameters and decoherence mechanisms affect the behavior of the emitter and of the driving field. To that end, we use the Hamiltonian of equation 2.22 to simulate the behavior of the transmitted light as a function of the parameters that characterize the emitter and its environment.

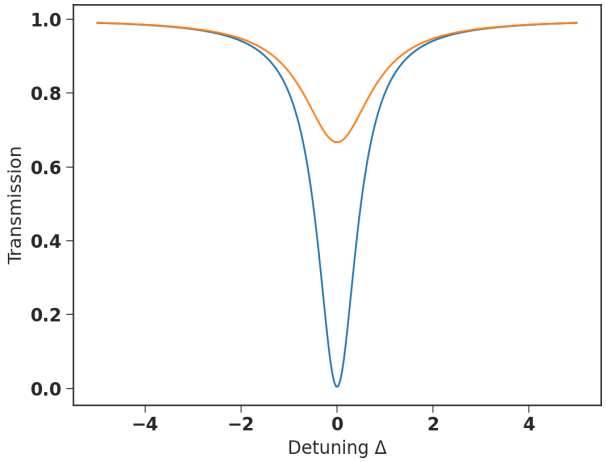

Figure 2.9: Transmission dips for an ideal system, where $\beta = 1$ and $\gamma_{deph} = 0$, for two different values of Rabi frequency, $\Omega_{blue} < \Omega_{orange}$. We note that not only the transmission dip decreases with the increased Rabi frequency, but we also observe broadening of the dip.

Firstly, we recognise the special case of having perfect coupling to the waveguide modes and no decoherence mechanisms present, meaning that $\beta = 1$ and $\gamma_{deph} = 0$, in the low power limit. In this case, the coherent extinction is maximum and we can see in Figure 2.9 the transmission dip reaching zero. This is the ideal case of the TLS fully reflecting the single photons that impinge on it, since in the low power limit the coherent component of the transmission dominates, the coherences don't decay as there is no dephasing and the scattered photons remain in the waveguide.

The effect of decoherence can be seen in Figure 2.10 (left plot), where the transmission on resonance has been plotted for perfect coupling $\beta = 1$ and for very low coupling $\beta = 0.2$. Decoherence results in fewer coherently scattered photons and consequently higher transmission on resonance, as the interference is decreased. Finally, in Figure 2.10 (right plot) the saturation of the quantum emitter is demonstrated, as for high values of excitation power per emitter lifetime, more photons of the incident field pass right through the emitter without interacting with it.

There is a plethora of mechanisms that broaden and/or shift the transition energy between the two levels of the QD. They can be due to phonons, which are lattice vibrations of the medium or due to carriers in the environment. As stated earlier in this chapter, phonons cause pure dephasing which results in

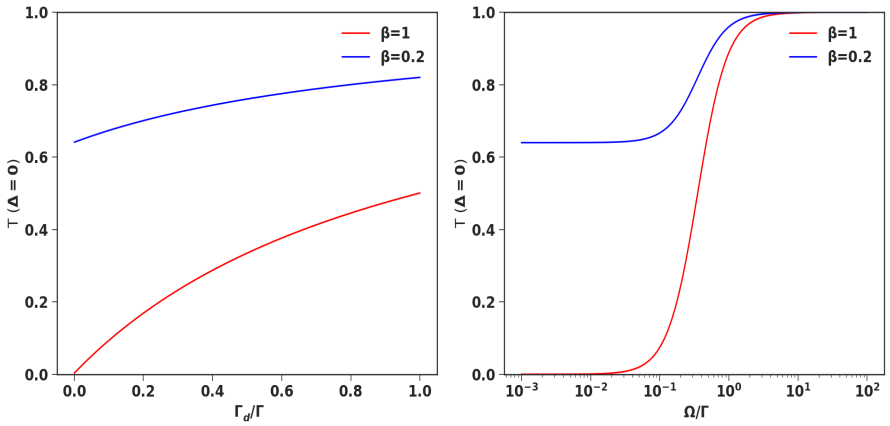

Figure 2.10: Transmission on resonance as a function of dephasing rate per emitter lifetime (plot on the left) and as a function of mean photon flux per emitter lifetime. Plotted both for $\beta = 1$ and $\beta = 0.2$.

decoherence, a highly undesired effect. More specifically, the coupling between the excitons of the QD and the phonons can result in sidebands in the emission spectrum and broadening of the ZPL line [22]. The decoherence induced by phonons happens in short time scales compared to the emitter's lifetime and is irreversible. It is very much dependent on the ambient temperature and on the degree of confinement. At cryogenic temperatures and 3D/0D confinement, decoherence is highly suppressed. However, this is not the case for 1D/2D confinement, where decoherence is enhanced by long-wavelength vibrations that can be significant even at sub-Kelvin temperatures. As decoherence is increased, the indistinguishability of the emitted photons is limited.

Additionally, carriers in the solid-state environment may induce an energy shift of the two level transition, known as *spectral diffusion*. This mechanism occurs at long time scales compared to the emitter lifetime and is reversible. Spectral diffusion is modelled as variations from the QD's resonant frequency by δ, such that $\omega_{sd} = \omega_0 + \delta$, and is described a Gaussian distribution with a mean value of zero and a width of σ_{sd} [21]

$$P(\delta) = \frac{1}{\sqrt{2\pi\sigma_{sd}^2}} e^{-\frac{\delta^2}{2\sigma_{sd}^2}}. \tag{2.37}$$

The model for the transmission has to be modified to include fluctuations from the transition by time averaging with the Gaussian of Equation 2.37.

$$T_{sd}(\Delta) = [T(\Delta) * P(\delta)] = \int d\delta T(\Delta - \delta) P(\delta). \tag{2.38}$$

3 Coherence functions and Visibility

In this chapter, the first and second order coherence functions will be described. The first order coherence function yields information about the spectral properties of the field according to the Wiener-Khinchin theorem and is connected to the visibility of interference fringes. The second order correlation function provides information about the photon statistics of the fields in an HBT setup. For the derivation of the correlation functions we will use the quantum regression theorem and input/output equations of the TLS [11]. Lastly, we will describe the two-photon time-energy entanglement analyzed using the Franson interferometer, consisting of two unbalanced Mach-Zehnder interferometers. The visibility of the two-photon component is used to predict the violation of the CHSH inequality, which can be used to certify two-photon entanglement.

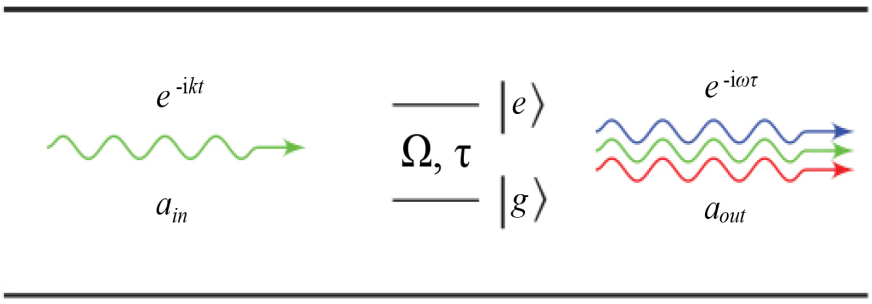

Figure 3.1: Two-level system with energy separation Ω and natural linewidth τ embedded in an chiral 1D-waveguide. With r_{in} and r_{out} we denote the incoming and outgoing electric fields. The blue, green and red outgoing fields represent the Mollow triplet of the strong driving regime, while in the weak we would only have the green. Figure is adapted from [11].

3.1 1st-order Coherence function

The 1st-order coherence function is given by the following equation

$$G^{(1)}(t,\tau) = \left\langle E^{(-)}(r,t)E^{(+)}(r,t+\tau)\right\rangle . \tag{3.1}$$

We shall start our analysis of $g^{(1)}$ for TLS embedded in a chiral waveguide, i.e. the light field can only propagate in one direction, as it is a simpler case and afterwards the analysis will be extended for a non-chiral waveguide.

3.1.1 Propagation in chiral waveguide

Our system is comprised of a two-level system embedded in a chiral 1D photonic waveguide, as shown in Figure 3.1, driven by a light field that can be described by a coherent state. The Hamiltonian of such a system is

$$
\begin{aligned}
H &= H_0 + H_1, \\
H_0 &= \int d\omega \omega a_\omega^\dagger a_\omega, \\
H_1 &= \frac{1}{2}\Omega\sigma_z + \frac{V}{\sqrt{u_g}} \int d\omega (\sigma_{ge} a_\omega + a_\omega^\dagger \sigma_{eg}),
\end{aligned}
\tag{3.2}
$$

where by ω we denote the frequency of the light field, a_ω and $a_\omega^\dagger$ are the annihilation and creation operators of the field at frequency ω, σ_{ge} and σ_{eg} the raising and lowering operators of the TLS such that $\sigma_z = [\sigma_{ge}, \sigma_{eg}]$, by V we denote the coupling strength between the atom states and the field at frequency ω and u_g is the group velocity of the propagating waveguide mode assuming linearized dispersion. Thus, the first term of the Hamiltonian expresses the energy of the field, the second the energy of the TLS and the third term is the interaction term.

We define the input and output fields as

$$
\begin{aligned}
r_{in}(t) = a_{in}(t) &= \frac{1}{\sqrt{2\pi}} \int d\omega a_\omega(t_0) e^{-i\omega(t-t_0)}, \\
r_{out}(t) = a_{out}(t) &= \frac{1}{\sqrt{2\pi}} \int d\omega a_\omega(t_1) e^{-i\omega(t-t_1)},
\end{aligned}
\tag{3.3}
$$

where t_0 and t_1 represent times long before and after, respectively, of the interaction with the atom. The fields are related by

$$
a_{out}(t) = a_{in}(t) - i\sqrt{\frac{2}{\tau}}\sigma_{eg}(t), \tag{3.4}
$$

where $\tau = u_g/\pi V^2$ is the natural linewidth of the TLS transition. Using the Heisenberg equations of motion, we can write the input/output relations for an atom interacting with a light field

$$\begin{aligned}
\frac{d\sigma_{eg}(t)}{dt} &= i\sqrt{\frac{2}{\tau}}\sigma_z(t)a_{in}(t) - (\frac{1}{\tau} + i\Omega)\sigma_{eg}(t), \\
\frac{d\sigma_{ge}(t)}{dt} &= -i\sqrt{\frac{2}{\tau}}\sigma_z(t)a^\dagger_{in}(t) - (\frac{1}{\tau} - i\Omega)\sigma_{ge}(t), \\
\frac{d\sigma_z(t)}{dt} &= -i2\sqrt{\frac{2}{\tau}}[\sigma_{ge}(t)a_{in}(t) - \sigma_{eg}(t)a^\dagger_{in}(t)] - \frac{2}{\tau}[\sigma_z(t) + 1],
\end{aligned} \tag{3.5}$$

We consider a coherent state of frequency k

$$|\alpha^+_k\rangle = e^{-|\alpha_k|^2/2}\sum_{n=0}^{\infty}\frac{\alpha^n_k a^{\dagger}_{in}k^n}{n!}|0\rangle\,, \tag{3.6}$$

such that

$$\begin{aligned}
a_{in}(t)\,|\alpha^+_k\rangle &= \frac{1}{2\pi}\int dk' a_{in}(k')e^{-ik't}\,|\alpha^+_k\rangle \\
&= \frac{\alpha_k}{\sqrt{2\pi}}e^{-ikt}\,|\alpha^+_k\rangle = \frac{\omega_R}{2}\sqrt{\frac{\tau}{2}}e^{i\phi-ikt}\,|\alpha^+_k\rangle\,,
\end{aligned} \tag{3.7}$$

where $\omega_R = 2|\alpha|/\sqrt{\pi\tau}$ is the Rabi frequency.

In order to describe the spectral properties and the statistics of the reflected and transmitted fields we need to be able to calculate the following three classes of correlation functions:

$$c_1(t=0,t') = \begin{pmatrix} \langle\sigma_{eg}(t)\rangle \\ \langle\sigma_{ge}(t)\rangle \\ \langle\sigma_z(t)\rangle \end{pmatrix} \tag{3.8}$$

$$c_2(t,t') = \begin{pmatrix} \langle \sigma_{ge}(t)\sigma_{eg}(t')\rangle \\ \langle \sigma_{ge}(t)\sigma_{ge}(t')\rangle \\ \langle \sigma_{ge}(t)\sigma_{z}(t')\rangle \end{pmatrix} \tag{3.9}$$

$$c_3(t,t') = \begin{pmatrix} \langle \sigma_{ge}(t)\sigma_{eg}(t')\sigma_{eg}(t)\rangle \\ \langle \sigma_{ge}(t)\sigma_{ge}(t')\sigma_{eg}(t')\rangle \\ \langle \sigma_{ge}(t)\sigma_{z}(t')\sigma_{eg}(t')\rangle \end{pmatrix} \tag{3.10}$$

In order to calculate the correlation functions of equations 3.8 - 3.10, we use the input/output equations of the TLS (3.5), we multiply from left and/or right with the suitable terms and then compute the expectation value. Also, we use equation 3.7 and the commutator $[a_{in}(t'), \sigma_{eg}(t)] = 0$ for $t' \gg t$ to derive the following set of differential equations for all three necessary classes of correlation functions, the so-called *optical Bloch equations with radiative damping*.

$$\frac{d}{dt'} c_n(t,t') = B(t')c_n(t,t') + b_n, \tag{3.11}$$

where

$$B = \begin{pmatrix} -(\frac{1}{\tau} + i\Omega) & 0 & \frac{i}{2}\omega_R e^{-ikt} e^{i\phi} \\ 0 & -(\frac{1}{\tau} - i\Omega) & -\frac{i}{2}\omega_R e^{ikt} e^{-i\phi} \\ i\omega_R e^{ikt'} e^{-i\phi} & -i\omega_R e^{-ikt'} e^{i\phi} & -\frac{2}{\tau} \end{pmatrix} \tag{3.12}$$

and

$$b_n = \begin{pmatrix} 0 \\ 0 \\ b_n \end{pmatrix} \tag{3.13}$$

where

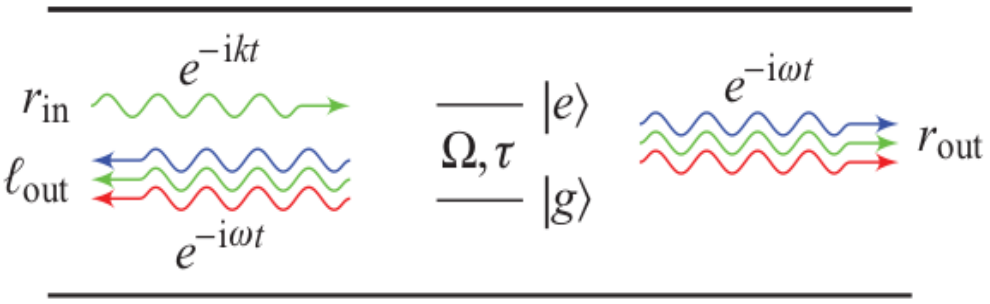

Figure 3.2: Two-level system with energy separation Ω and natural linewidth τ embedded in a non-chiral 1D-waveguide. With r_{in} we denote the incoming electric field. With l_{out} and r_{out} we denote the reflected and transmitted, respectively, outgoing electric fields. The blue, green and red outgoing fields represent the Mollow triplet of the strong driving regime, while in the weak we would only have the green. Figure is adapted from [11].

$$
\begin{aligned}
b_1 &= -\frac{2}{\tau}, \\
b_2 &= -\frac{2}{\tau} \langle \sigma_{ge}(t) \rangle , \\
b_3 &= -\frac{2}{\tau} \langle \sigma_{ge}(t) \sigma_{ge}(t) \rangle .
\end{aligned}
\tag{3.14}
$$

The results derived above are usually derived in the bibliography by the use of the quantum regression theorem, however here we only used the relations between input and output fields for the calculation.

3.1.2 Propagation in non-chiral waveguide

In this section, we shall extend our analysis to a TLS embedded in a non-chiral 1D photonic crystal waveguide, such as the system depicted in Figure 3.2. In this case, we can decompose the right and left going input or output states

$$
\begin{aligned}
r_{in/out}(t) &= \frac{a_{in/out}(t) + \mathring{a}_{in/out}(t)}{\sqrt{2}}, \\
l_{in/out}(t) &= \frac{a_{in/out}(t) - \mathring{a}_{in/out}(t)}{\sqrt{2}}.
\end{aligned}
\tag{3.15}
$$

As a result, the Hamiltonian of the system can be written as

$$
\begin{aligned}
H &= H_0 + H_1, \\
H_0 &= \int d\omega \omega (a_\omega^\dagger a_\omega + \mathring{a}_\omega^\dagger \mathring{a}_\omega), \\
H_1 &= \frac{1}{2}\Omega\sigma_z + \sqrt{2}\frac{V}{\sqrt{u_g}} \int d\omega (\sigma_{ge} a_\omega + \sigma_{eg} a_\omega^\dagger).
\end{aligned}
\tag{3.16}
$$

The fields a and $\mathring{a}$ are even and odd combinations of the right and left propagating fields. H_0 is the free Hamiltonian of the field and H_1 represents the interaction between the electric field and the TLS.

A right going coherent state of frequency k can be written as:

$$
|\alpha\rangle = \exp\Big\{\alpha r_{in}^\dagger(k) - \alpha^\star r_{in}(k)\Big\} |0\rangle \,. \tag{3.17}
$$

We can decompose this into two channels, even and odd

$$
\begin{aligned}
|\alpha\rangle &= \exp\left\{\alpha \frac{a_{in}^\dagger(k) + \mathring{a}_{in}^\dagger(k)}{\sqrt{2}} - \alpha^\star \frac{a_{in}(k) + \mathring{a}_{in}(k)}{\sqrt{2}}\right\} |0\rangle \\
&= |\frac{\alpha_k^+}{\sqrt{2}}; \frac{\alpha_k^+}{\sqrt{2}}\rangle \,,
\end{aligned}
\tag{3.18}
$$

where the first and second terms represent the even and odd channels such that

$$
\begin{aligned}
a_{in}(t)\,|\frac{\alpha_k^+}{\sqrt{2}};\frac{\alpha_k^+}{\sqrt{2}}\rangle &= \mathring{a}_{in}(t)\,|\frac{\alpha_k^+}{\sqrt{2}};\frac{\alpha_k^+}{\sqrt{2}}\rangle = \mathring{a}_{out}(t)\,|\frac{\alpha_k^+}{\sqrt{2}};\frac{\alpha_k^+}{\sqrt{2}}\rangle \\
&= \frac{\alpha_k}{2\sqrt{\pi}}e^{-ikt}\,|\frac{\alpha_k^+}{\sqrt{2}};\frac{\alpha_k^+}{\sqrt{2}}\rangle \\
&= \frac{\omega_R}{2}\sqrt{\frac{\tau'}{2}}e^{i\phi-ikt}\,|\frac{\alpha_k^+}{\sqrt{2}};\frac{\alpha_k^+}{\sqrt{2}}\rangle\,,
\end{aligned}
\tag{3.19}
$$

where $\tau' = \tau/2$ and τ is the natural linewidth of the TLS.

The first order coherence function of the transmitted field can be calculated by

$$
\left\langle r_{out}^\dagger(t) r_{out}(t+\delta t)\right\rangle = \frac{1}{2}\left\langle [a_{out}^\dagger(t) + \mathring{a}_{out}^\dagger(t)][a_{out}(t+\delta t) + \mathring{a}_{out}(t+\delta t)]\right\rangle . \tag{3.20}
$$

The output and input fields are related by Equation 3.4, which we combine with Equation 3.20 and we get that the first order coherence function is given by

$$
\begin{aligned}
&= \omega_R^2\frac{\tau'}{4}e^{-ik\delta t} - \frac{i}{2}\omega_R e^{-i\phi+ikt}\,\langle\sigma_{eg}(t+\delta t)\rangle \\
&+ \frac{i}{2}\omega_R e^{-i\phi+ik(t+\delta t)}\,\langle\sigma_{ge}(t)\rangle \\
&+ \frac{1}{\tau'}\,\langle\sigma_{ge}(t)\sigma_{eg}(t+\delta t)\rangle
\end{aligned}
\tag{3.21}
$$

It can be shown that the two-channel expectation values are the same as their single channel analogues, thus we can use the Bloch equations derived for propagation in chiral waveguide for the case of the non-chiral. The whole derivation won't be presented here, but rather the steady state solutions in the frequency domain.

We decompose the correlation function to two parts, its coherent $\omega = k$, and its incoherent, $\omega \neq k$. The incoherent part is the same for the transmitted and reflected fields, but the coherent differs.

$$
\begin{aligned}
g^{(1)}_{t,coh} &= \frac{1}{1 + D^2 + \frac{1}{2}R^2}(D^2 + \frac{1}{2}R^2\frac{D^2 + \frac{1}{2}R^2}{1 + D^2 + \frac{1}{2}R^2}), \\
g^{(1)}_{r,coh} &= \frac{1 + D^2}{1 + D^2 + \frac{1}{2}R^2}, \\
g^{(1)}_{incoh} &= \frac{1}{\pi}\frac{1}{1 + D^2 + \frac{1}{2}R^2}\frac{R^2}{\tau'^5}\frac{(\omega - k)^2\tau'^2 + 4 + \frac{1}{2}R^2}{|P[-i(\omega - k)]|^2},
\end{aligned}
\tag{3.22}
$$

where

$$
\begin{aligned}
D &= (\Omega - k)\tau', \\
R &= \omega_R\tau'.
\end{aligned}
\tag{3.23}
$$

The coherent and incoherent spectrum of the transmitted and reflected fields are shown in Figure 3.3.

3.1.3 Visibility

The visibility of interference fringes is defined as [6]

$$
V = \frac{I_{max} - I_{min}}{I_{max} + I_{min}},
\tag{3.24}
$$

where

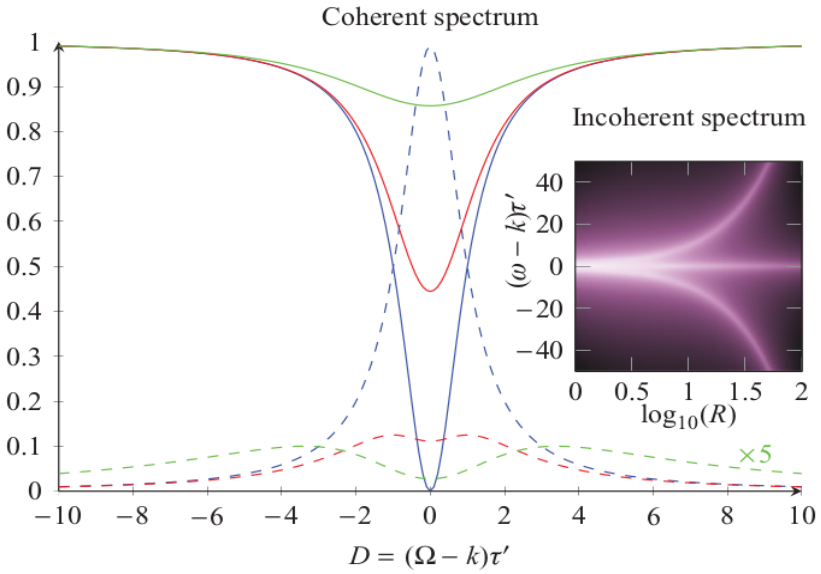

Figure 3.3: Coherent spectrum of the transmitted and reflected fields. Transmitted field is plotted with solid lines and the reflected with dashed. $R = 0.1, 2, 5$ shown in blue, red and green, respectively. In the inset, the incoherent spectrum is shown with the Mollow triplet for zero detuning. Figure taken from [11].

$$I_{max/min} = I_1 + I_2 \pm 2\sqrt{I_1 I_2}|g^{(1)}(x_1, x_2)|, \tag{3.25}$$

where I_1 and I_2 are the intensities measured by detectors at the positions x_1, x_2.

Therefore, the visibility is related to the 1st-order coherence function as

$$V = \frac{2\sqrt{I_1 I_2}|g^{(1)}(x_1, x_2)|}{I_1 + I_2}, \tag{3.26}$$

meaning that, both in classical and in quantum physics, in order to observe interference the light must be temporally and spatially coherent and since they are proportional, the higher the coherence of the light, the higher the visibility and vice versa.

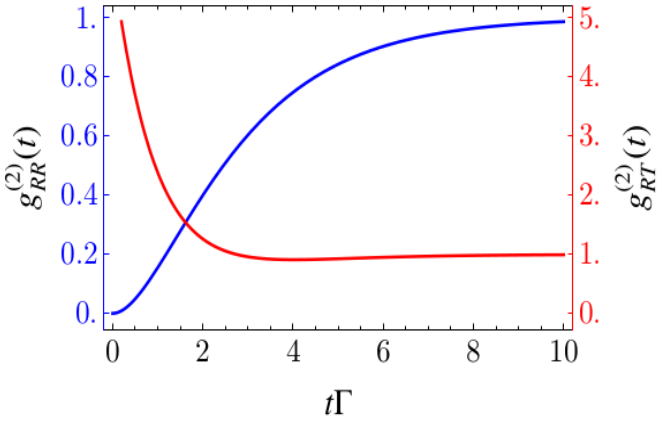

Figure 3.4: Blue: 2nd-order coherence function of the reflected field. We notice that the zero-time $g^0_{RR} = 0$, meaning that the quantum dot reflects only single photons. Red: Correlations occur between the reflected and transmitted components. The bunched statistics of the transmitted field overtake the antibunched nature of the reflected for zero-time. Both the coherence functions decay to 1 for a longer time delay. Figure taken from [21].

3.2 2nd-order Coherence function

An analytical expression for the $g^{(2)}(\tau)$ can be derived only in the limit of $\Omega_R/\gamma \ll 1$ or $\Delta = 0$. The derivation is not the focus of this work, but it follows the same procedure followed for $g^{(1)}$ or we can use the quantum regression theorem and then take the Laplace transform. The final expressions for the 2nd-order coherence function of the transmitted and the reflected field will be presented here; [21].

$$g^{(2)}_T(\tau) = 1 + \frac{\gamma^2\gamma_2\beta^4 e^{-\gamma\tau} - \gamma\beta^2[2\gamma_2 + \gamma(\beta-2)]^2 e^{-\gamma_2\tau}}{(\gamma-\gamma_2)[2\gamma_2+\gamma\beta(\beta-2)]^2}, \tag{3.27}$$

$$g^{(2)}_R(\tau) = 1 - \frac{\gamma e^{-\tau\gamma_2} - \gamma_2 e^{-\tau\gamma}}{\gamma-\gamma_2}. \tag{3.28}$$

Notice that $g^{(2)}_R(\tau)$ is independent of the coupling to the waveguide, β. The beta factor, doesn't influence the statistics of the reflected field, but merely reduces the its intensity as photons escape out of the waveguide for $\beta < 1.0$. The

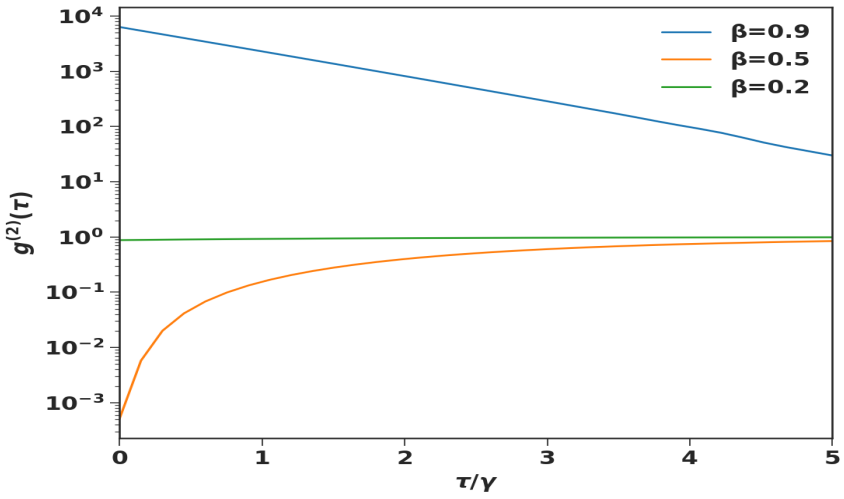

Figure 3.5: 2nd order coherence function of the photons in the transmitted mode as a function of delay time per lifetime. Three different cases are under investigation depending on the degree of coupling, $\beta = 0.9$, $\beta = 0.5$ and $\beta = 0.2$. We observe that for very good coupling, $\beta = 0.9$, the statistics show bunching, for $\beta = 0.5$ we have antibunching and for $\beta = 0.2$ coherent statistics.

zero-delay 2nd order coherence function is zero, $g_R^{(2)} = 0$, for any dephasing rate, demonstrating that in the low-power limit and close to resonance, the quantum dot only reflects single photons.

In the special case of no pure dephasing, $\gamma_{deph} = 0$, then $g_T^{(2)}$ reduces to

$$g_T^{(2)}(\tau) = e^{-\gamma\tau}\left(\frac{\beta^2}{(1-\beta)^2} - e^{-\frac{\gamma_2}{2}\tau}\right)^2. \tag{3.29}$$

The $g_T^{(2)}$ is plotted against the delay time per emitter lifetime τ/γ in the absence of dephasing in Figure 3.5. When the emitter is well coupled, the $g_T^2 > 1$ and in this case the transmitted mode photons are bunched. In the case of very low power, the transmitted photons are photon pairs ideally. On the contrary, when $\beta = 0.5$, both the reflection and the transmission is made of single photons and the statistics are antibunched. Lastly, when the emitter-waveguide coupling is too low, the photons don't interact with the quantum dot and as such we observe the statistics of a weak coherent beam, for which we know that $g^{(2)}(\tau) = 1$.

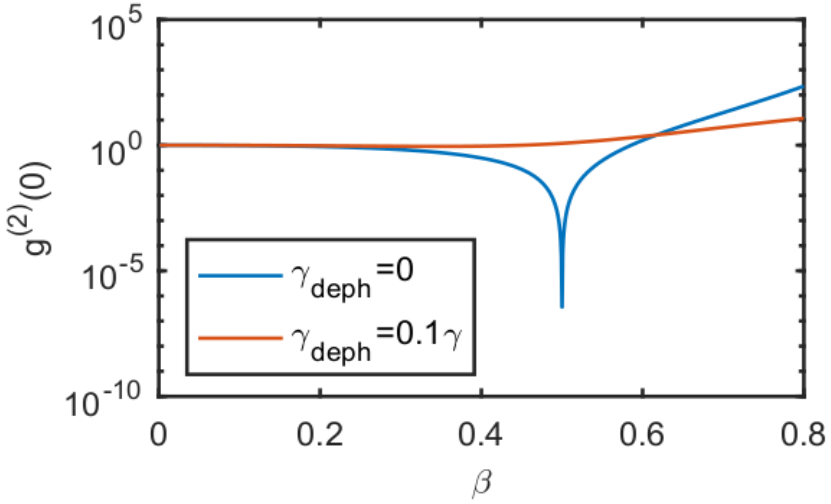

Figure 3.6: Zero-delay time 2nd order coherence function of the photons in the transmitted mode as a function of waveguide-emitter coupling, β. Efficient coupling is crucial for the observation of bunched and antibunched statistics. Figure taken from [12].

The zero-delay time $g_T^{(2)}$ is plotted as a function of the waveguide coupling efficiency, β, in Figure 3.6. It demonstrates the necessity of efficient coupling for the observation of bunched and antibunched statistics and the influence of the dephasing on them. In the absence of dephasing, *blue line*, we see that for coupling close to $\beta = 0.5$ the photon statistics are antibunched. This means that both the reflected and the transmitted modes of the waveguide are governed by single photons. As the coupling efficiency grows larger, the statistics are becoming bunched. This is a consequence of the interference between the scattered photons, that as β is increased couple more efficiently into the waveguide, and the emitted photon field.

3.2.1 Effect of decoherence on 2nd-order coherence function

Pure dephasing mechanisms cause decay of the coherences σ_{eg}, σ_{ge}, of the TLS. This results in loss of coherence in the scattered field and it has a high impact

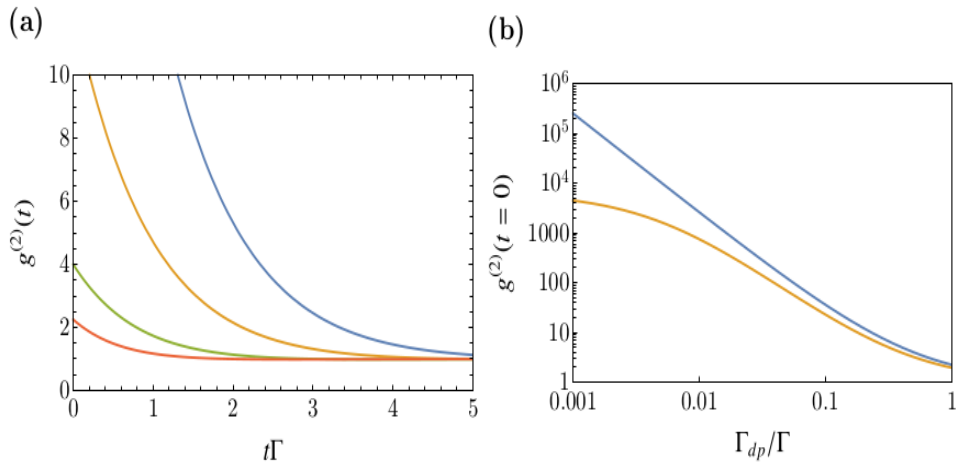

Figure 3.7: (a) 2nd order coherence function of the photons in the transmitted mode as a function of delay time τ in the presence of dephasing. Red, green, orange, blue correspond to $\gamma_d/\gamma = 1, 0.5, 0.2, 0.1$ respectively, plotted in the low power limit and for $\beta = 1$. (b) Zero-delay time 2nd order coherence function of the photons in the transmitted mode as a function of the dephasing rate per emitter lifetime γ_d/γ in the low power limit. The blue curve is plotted for $\beta = 1$ and the orange for $\beta = 0.9$. Figure taken from [21].

on the behavior of the system TLS-light field. Specifically, the photon statistics of the transmitted field are highly influenced by the pure dephasing.

The influence of dephasing is demonstrated in Figure 3.7. In (a) we can see the influence of various dephasing rates on the second order coherence function in the ideal case of perfect coupling, $\beta = 1$. For a large dephasing rate, the coherences of the system decay faster and as such, the field in the transmitted mode is not exclusively made of two-photon states. For $\gamma_d/\gamma = 1$ (red) we see that $g^{(2)}(0)$ is a bit larger than 2, indicating that the dephasing almost destroys the bunched photon statistics. In (b) we see the dependence of the zero-delay time 2nd order coherence function $g^{(2)}(0)$ on the dephasing rate per emitter lifetime. Even if $\gamma_d/\gamma = 0.01$, then $g^{(2)}(0)$ is reduced by approximately 90%.

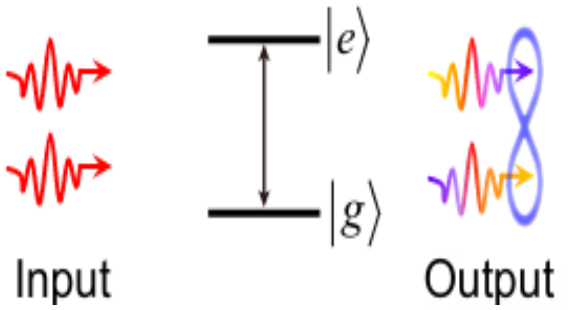

Figure 3.8: 2-photon inelastic scattering by the TLS. The uncertainty in the energy of the emitted photons simultaneously with the energy conservation of the process gives rise to correlations.

3.3 Time-energy entanglement

In the weak driving regime, we can approximate the light field as a weak coherent state, as in Equation 1.1. The two-photon component of the driving field can be elastically or inelastically scattered by the emitter. The energy is conserved in both cases and in the case of inelastic scattering, $2\omega_p = \omega_1 + \omega_2$, where ω_p is the frequency of the pump photons and ω_1, ω_2 are the frequencies of the emitted photons, the emitted photons inherit an uncertainty in energy which is proportional to $1/\tau$. The two-photon emitted state can be written as:

$$
\begin{aligned}
|\psi_2\rangle = & \int d\omega_1^{in} d\omega_2^{in} f(\omega_1^{in}) f(\omega_2^{in}) \\
& \int d\omega_1 d\omega_2 [\chi(\omega_1^{in}) \chi(\omega_2^{in}) \delta(\omega_1 - \omega_1^{in}) \delta(\omega_2 - \omega_2^{in}) \\
& + \frac{1}{2} T_{\omega_1^{in} \omega_2^{in} \omega_1 \omega_2} \delta(\omega_1 + \omega_2 - \omega_1^{in} - \omega_2^{in})] \, |1_{\omega_1} \, |1_{\omega_2}\rangle\rangle,
\end{aligned}
\tag{3.30}
$$

where $\chi(\omega_1^{in}), \chi(\omega_2^{in})$ represent independent scattering events, with each photon conserving its own energy [13].

For a laser with a narrow linewidth $\omega_1^{in} = \omega_2^{in} = \omega_p$ and $f(\omega) = \delta(\omega - \omega_p)$ and so we can write the two-photon state as:

$$
\begin{aligned}
|\psi_2\rangle &= \frac{1}{2}\int d\omega_1 d\omega_2 T_{\omega_p\omega_p\omega_1\omega_2}\delta(\omega_1+\omega_2-2\omega_p)\,|1_{\omega_1}\,|1_{\omega_2}\rangle\rangle \\
&= \frac{1}{2}\int d\omega_1 T_{\omega_p\omega_p\omega_1 2\omega_p-\omega_1}\,|1_{\omega_1}\,|1_{2\omega_p-\omega_1}\rangle\rangle,
\end{aligned}
\tag{3.31}
$$

The term $T_{\omega_p\omega_p\omega_1\omega_2}$ expresses the scattering matrix of the emitter, including the spectral entanglement. For a quantum dot embedded in a waveguide, the scattering matrix is given by the following expression

$$
\begin{aligned}
T_{\omega_p\omega_p\omega_1 2\omega_p-\omega_1} &= \frac{4}{\pi\beta\Gamma}\frac{r(\omega_1^{in})r(\omega_2^{in})r(\omega_1)r(\omega_2)}{r((\omega_1^{in}+\omega_2^{in})/2)} \\
&= \frac{4}{\pi\beta\Gamma}r(\omega_p)r(\omega_1)r(2\omega_p-\omega_1).
\end{aligned}
\tag{3.32}
$$

We can use the reflection and transmission coefficients, in the absence of dephasing, and on resonance $\omega_p = \omega_0$, we can write the scattering matrix as

$$
\begin{aligned}
T_{\omega_p\omega_p\omega_1 2\omega_p-\omega_1} &= -\frac{4}{\pi}r(\omega_1)r(2\omega_p-\omega_1) \\
&= -\frac{4\beta^2}{\pi\gamma(1-2i\Delta/\gamma)(1+2i\Delta/\gamma)},
\end{aligned}
\tag{3.33}
$$

where $\Delta = \omega_1 - \omega_p$ is the detuning between the driving photons and the emitted photons. The final expression for the scattering matrix is the following

$$
T_\Delta = -\frac{4\beta^2}{\pi\gamma(1+4\frac{\Delta^2}{\gamma^2})},
\tag{3.34}
$$

which contains all the spectral information given by the Lorentzian profile. The two-photon state can be written as

$$
|\psi_2\rangle = \frac{1}{2}\int d\Delta T_\Delta\,|1_\Delta\rangle\,|1_{-\Delta}\rangle.
\tag{3.35}
$$

The state written in this form clearly demonstrates the energy correlation between the two photons.

The joint time distribution of the driving photons and the emitted photons can be described in terms of the two-photon amplitude

$$\begin{aligned} A(t,t') &= \langle 0,0|\, E_1^{(+)}(0,t) E_2^{(+)}(0,t')\, |\psi_2\rangle = \\ &= \int d\omega_1 a_{\omega_1} e^{-i\omega_1 t} \int d\omega_2 a_{\omega_2} e^{-i\omega_2 t'} \int d\Delta T_\Delta a^\dagger_{\omega_p+\Delta} a^\dagger_{\omega_p-\Delta} \,|0\rangle \\ &= \int d\Delta e^{-i(\omega_p+\Delta)t'} e^{-i(\omega_p-\Delta)t'} T_\Delta \\ &= e^{-i\omega_p t} e^{-i\omega_p t'} \int d\Delta e^{i\Delta(t-t')} T_\Delta. \end{aligned} \tag{3.36}$$

The last integral represents the Fourier transform of the two-photon spectral amplitude. Each of the photons has a Lorentzian profile and thus the Fourier transform of their multiplication would be the same as the convolution of their individual Fourier transforms. Therefore, the two-photon correlation function [3.36] will be a double-exponential decay with a linewidth proportional to $1/\gamma$.

3.3.1 Franson interferometry

To probe the properties of time-energy entanglement of the two photon state, we can use the Franson interferomter [5]. It consists of two identical UMZI to which two photons can go. The control of the phase difference between the two interferometers and two photon detection at the outputs of each interferometer can be used to probe properties of the time-energy entangled state and can be used to test of local hidden-variable theories probing the Bell theorem. For this the CHSH ineqaulity violation can be used [4]. The visibility V extracted from the two photon correlations can be used to estimate the S parameters that can be achieved with the setup.

$$S = 2\sqrt{2}V \tag{3.37}$$

If $S > 1/\sqrt{2}$ then the state is entangled and if $S > 2$ the state does not obey local realism.

The coincidence count rate measured between the two detectors is proportional to:

$$R_c(t,t') \propto \langle 0| E^\dagger(r,t')E^\dagger(r,t)E(r,t)E(r,t') |0\rangle . \tag{3.38}$$

The interferometer introduces a time delay δt which transforms the electric field amplitudes as

$$E(r,t) -> \frac{1}{2}(E_i(r,t) + e^{i(\phi_1+\phi_2)}E(r,t-\delta t)). \tag{3.39}$$

Thus we can rewrite the coincidence count rate as

$$R_c(t,t') \propto \frac{1}{16}\langle 0| (E(r',t)E(r,t) + e^{-i(\phi_1+\phi_2)}E(r',t-\delta t)E(r,t-\delta t) + h.c.) |0\rangle . \tag{3.40}$$

The uncertainty of the individual photons ω_1 and ω_2 is much larger than the total energy $\omega_1 + \omega_2$ uncertainty and so we can write

$$E(r',t-\delta t)E(r,t-\delta t) |0\rangle = e^{i\omega_p \delta t}E(r',t)E(r,t) |0\rangle . \tag{3.41}$$

The phase factors introduced by the UMZIs is the reason we observe interference in the coincidence count rate

$$R_c(t,t') \propto (1+e^{-i(\omega_p \delta t+\phi_1+\phi_2)})(1+e^{i(\omega_p \delta t+\phi_1+\phi_2)}) = \frac{1}{2} + cos(\omega_p \delta t + \phi_1 + \phi_2). \tag{3.42}$$

It should be noted here, that the reason we don't observe interference due to the elastically scattered two-photon component is that the total energy uncertainty is equivalent to the uncertainty of the individual photons.

4 Mach-Zehnder interferometer

A substantial part of this work was the construction of an unbalanced Mach-Zehnder interferometer, drawn in Figure 4.1. It is constructed in such a way that it can be used to probe the interference of the quantum state of light that we insert into it or to control the relative phase between laser pulses that can be used to excite the quantum dot. In this work, the interferometer was used to interfere the light from the transmitted or the reflected mode and measure the visibility as a function of the excitation power. Additionally, it was used to estimate if the CHSH inequality would be violated by the two-photon state of the transmitted mode by measuring the visibility of the coincidences.

4.1 Interferometer description

As we can see, the interferometer has two inputs. One of them is used to insert light from the cryostat and investigate its interference pattern, we denote this path as the *detection path*. The second input can be used either for phase stabilization or for excitation of the quantum dot, *stabilization/excitation path*. For the purposes of the experiments discussed here, the *stabilization path* was used to set and stabilize the phase of the interferometer. All the optical fiber adapters are cage mounted along with their collimation lenses for precise adjustment. The half-waveplates (HWP) and quarter-waveplates (QWP) are also cage mounted and can be automatically rotated in order to change the polarization of the light beam. It should be noted that the propagation path along the translation stage is referred to as *long path* and the one passing through the beamsplitters as *short path*. Two mirrors are mounted on the translation stage with a maximum path length difference of 1m. The path length of 1m is chosen such that we can distinguish between short and long paths. One of the two mirror mounts of the mirrors on the translation stage is attached to a PZT and thus we can set and stabilize the phase of the interferometer.

4.1.1 Detection path

As detection path we are referring to the propagation path that inputs light from the cryostat that ends up fiber coupled and led to photon detectors. The light from the cryostat is brought to the interferometer via an optical fiber. The optical fiber is a single mode optical fiber in combination with an aspheric collimation lens of f=11mm. Afterwards, the beam goes through

HWP1 and QWP1. The role of those components is to allow us to change the polarization of the incoming light, as they are mounted on rotation mounts. As a result, we have an adjustable power ratio of the intensity going through each arm of the interferometer, since it is split by a polarizing beam splitter (PBS1). The vertical polarization component of the beam is transmitted, while the orthogonal is reflected when the beam passes through the beamsplitter. HWP1 and QWP1 were rotated such that the light was linearly polarized at 45° and thus the beam intensity was split in half after propagation through PBS1. The orthogonal component of the beam propagates through the long path, acquiring a relative phase in relation to the vertical polarization, proportional to the difference in path length. A constant phase shift is introduced by the fixed path length difference and also a variable phase proportional to the difference in path length owed to the movement of the mirror mounted on the piezo-mount. After reflection by the mirrors, the long path beam passes through a HWP that is rotated by 45° so that the polarization of the beam is rotated by 90°, setting the polarization from orthogonal to vertical. That is necessary as the beams must be by all aspects as similar as possible so that interference occurs. The two beams overlap at the 50:50 beamsplitter denoted as BS and then are coupled into optical fibers that are connected onto photon detectors. In order to observe (and maximize) interference fringes, the two separate beams must be in the same mode, spectrally, spatially and polarization-wise. The spatial overlap of the beams plays a very important role and it is very iterative process that has to be done perfectly to observe interference. It was achieved by precisely adjusting all the optical elements of the detection path, focusing mostly on the two mirrors on the translation stage, after numerous iterations. Finally, it should be noted here that after careful adjustment of the components, the collection efficiency at each arm from each path was between 65-75% and the visibility at each arm of the BS, was above 99%, as measured by each APDs placed at each detection arm.

4.1.2 Stabilization path

The light was brought to the interferometer via a polarization maintaining single mode optical fiber (PM fiber). Upon exiting the PM fiber, it passed

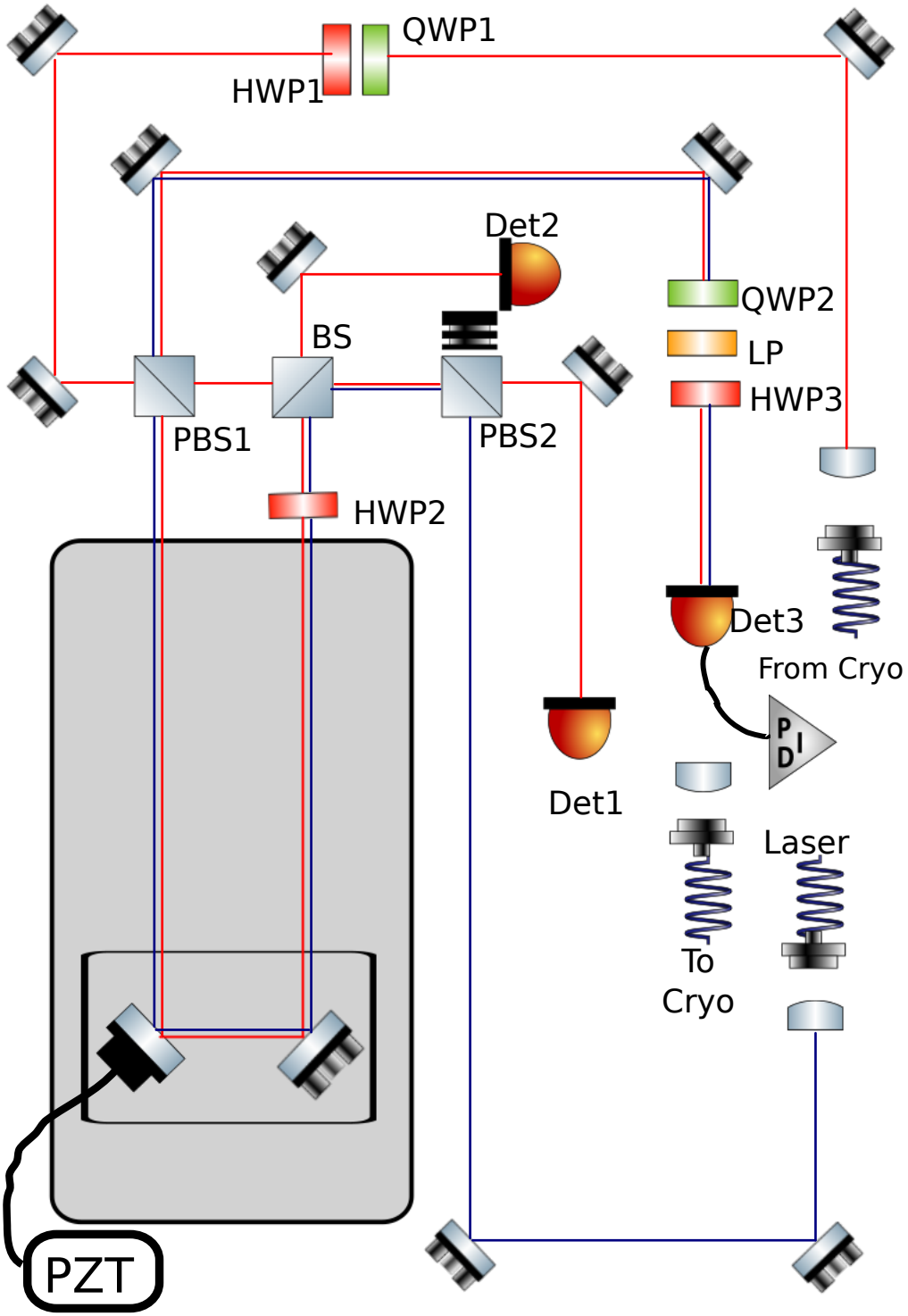

Figure 4.1: Schematic of the UMZI that was constructed. Light is inserted from optical fibers shown as: *From Cryo* and *Laser*. Det1 and Det2 are used to record interference, Det3 is used to stabilize the interferometer phase. The gray rectangle represents the translation stage, where on of the mirrors (left) is mounted on a PZT mount, to set and stabilize the phase.

through a collimation lens, of focal length f = 11mm. After being reflected by two mirrors, it was guided onto a PBS2 where the orthogonal polarization component was reflected and the vertical was transmitted. The orthogonal component of the beam was incident on the 50:50 BS where half of the photons go through the long path and the other half go through the short path. It should be noted here that the beam of the stabilization path was propagating in parallel to the detection path to minimise the overlap. The long path photons firstly pass through the HWP at 45°where their polarization becomes vertical and then are reflected by the mirrors. Same as for the case of the detection path, the photons that travel through the long path have undergone a phase shift proportional to the path length difference and the path length variation due to the PZT on the mirror mount. The long path beam is transmitted by PBS1 as it is vertically polarized at this point. On the other hand, the short path beam is reflected as it has orthogonal polarization and as such they both end up travelling in the same spatial mode. Finally, before coupling into the optical fiber or APD, the beams go through a series of polarization elements, namely a QWP, a linear polarizer and a HWP. The HWP is placed there in order to rotate the polarization of the beam and align it with the polarization axis of the PM fiber. The role of the QWP is to select the ratio of the long/short path intensity; it essentially acts as a variable polarizing beam splitter. The linear polarizer projects onto the linear polarisation defined by its orientation. The combination of the QWP at 45 °and rotating LP allows to vary the phase of the interference fringe as it defines the phase difference between two orthogonal polarisation propagating through different paths.

4.2 Interferometer stabilization and locking

Small fluctuations of the path length difference due to environmental noise can induce noise and instability of the interferometer, thus it was necessary to lock it usign the PZT that was connected to one of the mirror mounts on the translation stage. The locking technique we used is called *Lock-in amplification*. It is generally used when we have a noisy periodic signal. It removes the noise by multiplying the signal with another periodic signal called *reference signal* of the same frequency and then time average it. The noise will effectively be time averaged to zero and all that will be left will be the signal, which we finally amplify with low noise amplifiers.

In our case, the lock in amplification is implemented by a microcontroller [14]. We detect the interference signal using an APD, which is connected to one of the inputs of the FPGA of the microcontroller. The interference signal is then modified by the PID of the microcontroller and output to a piezo controller, which applies a voltage signal to our piezo mirror mount. By implementing this feedback process, essentially the piezo moves one of the mirrors of the translation stage such that the signal remains locked at a maximum or minimum value.

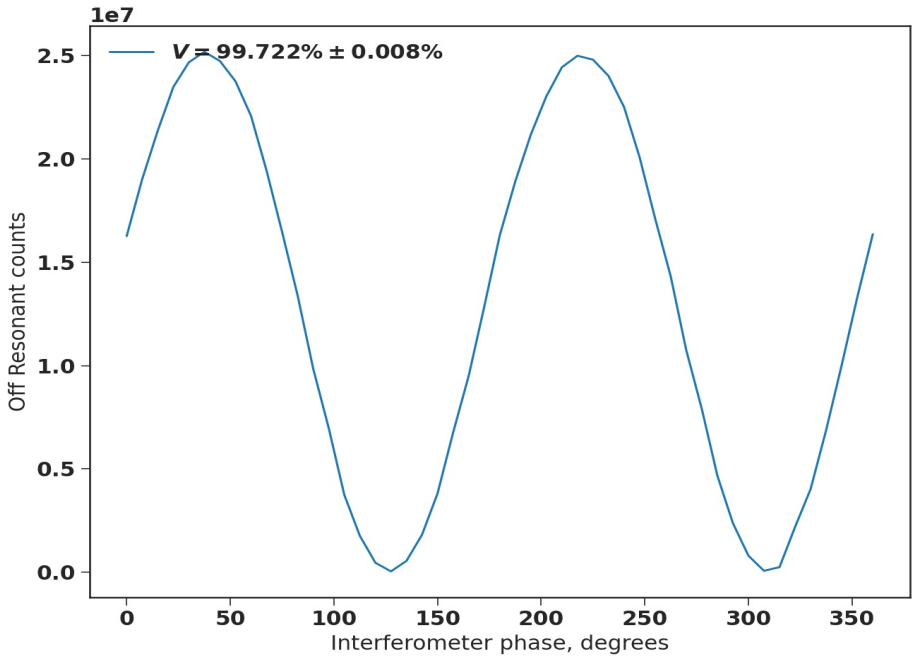

Figure 4.2: Photon counts measured by the photodetector as we scan the interferometer phase. We can see the interference fringes with a rather large visibility.

4.3 Interferometer operation

The rotation mounts of the polarizing elements at the end of the excitation path are motorized for precise and automated adjustment by the PC. The operation of the interferometer was fully automated and ran by a MATLAB program. The program changes the phase of the interferometer by rotating the linear polarizer and then tests if the interferometer is locked. If necessary, it relocks the interferometer. The resulting intensity on either of the detectors will be proportional to a sinusoidal function of the constant delay and of the phase induced by the piezo moving the mirror mount

$$I \propto sin(\phi_{\Delta l} + \phi_{LP}), \tag{4.1}$$

where $\phi_{\Delta l}$ would be the constant phase difference due to the path length difference of the short and long path and ϕ_{LP} the variable phase induced by the piezo. Then the visibility is given by

$$V = \frac{I_{max} - I_{min}}{I_{max} + I_{min}}. \tag{4.2}$$

An example of the interference fringes as we scan the phase of the interferometer can be viewed in Figure 4.2.

5 Experiments

In this chapter, the experiments and optical setups will be presented. Three experiments were conducted; one aimed to demonstrate the single photon non-linearity of the quantum dot and extract system parameters by applying a theoretical fit on the experimental data. The second made use of a double-pass Mach Zehnder type interferometer to investigate how the visibility of light that interacted with the quantum dot changes as a function of the laser power that drives it. The final experiment made use of two identical UMZIs to measure the visibility of the 2nd-order correlation function of the 2-photon component of the transmitted field in order to estimate the S parameter of the CHSH inequality and probe the time-energy entanglement introduced by interaction with the quantum dot.

5.1 Saturation of emitter

5.1.1 Characterization of quantum dot

The quantum dot allows for different fraction of the light to be transmitted, depending on the excitation power. For low powers, light is primarily reflected while for higher powers it is mostly transmitted until the quantum dot is saturated. In order to observe that phenomenon and to extract system parameters, we excited the quantum dot with a frequency tunable continuous-wave laser via one of the waveguide's grating couplers. The laser intensity was stabilized by passing through a PID feedback loop, employing an AOM double-pass configuration. The details of this technique are beyond the scope of this thesis, however the principle is the following: the acousto-optic modulator is used to modulate the intensity of the laser and to correct the intensity fluctuations (read by an avalanche photodetector) by driving the AOM with a correction signal determined by the photodiode signal and the proportional, integral and derivative components of the PID feedback circuit. The sample quantum dot was a self-assembled InGaAs quantum dot embedded in a one-dimensional photonic crystal waveguide, mounted in a cryogenic temperature environment ($T = 4K$) to suppress phonon-induced decoherence.

The range of the excitation power was from $1\mu W$ to $300\mu W$. The resonant frequency of the quantum dot shifts as the driving power changes, therefore for each value of laser power we scanned the laser frequency from 318.657GHz to 318.675GHz. In Figure 5.1 we can see how the resonant frequency changes with the driving power. Additionally, for each value of laser power and while scanning the laser frequency, the intensity of light transmitted by the quantum dot was recorded by a single photon counter module. We measured 30 different transmission curves, one for each value of the laser power, some of which can be seen in Figure 5.2 , while all of them can be viewed in the inset. The transmission curves approximate a Lorentzian with linewidth inherited by the quantum dot, proportional to γ_2, that is subject to power broadening [Eq 2.21]. The slight asymmetry of the transmission curves is due to the Fano

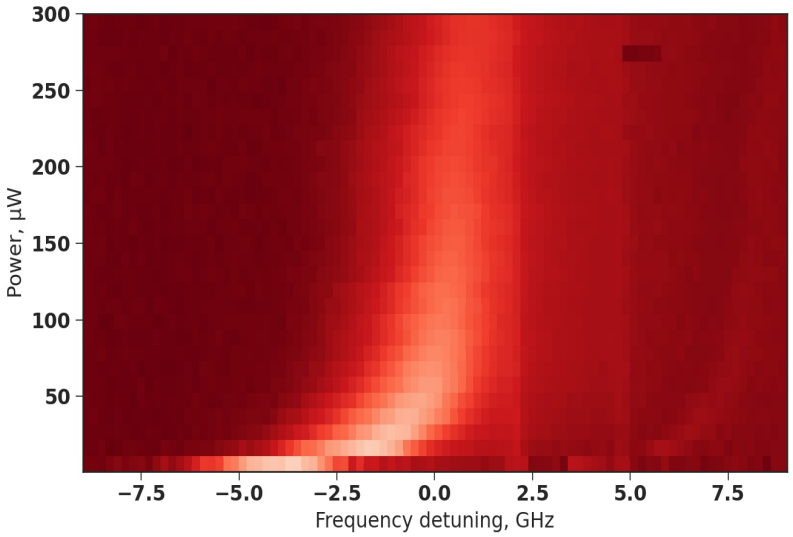

Figure 5.1: The quantum dot's resonant frequency shifts with the laser power. The detuning is measured as the frequency shift from the mean value of all recorded frequencies.

resonance, the effective existence of a low quality factor cavity created by weak reflections at the gratings of the waveguide. The dip of the transmission at $\Delta = 0$ is a signature of the quantum dot; the photons that are emitted by the quantum dot interfere destructively with the photons that are scattered by it. However, as the excitation power increases the aforementioned interference is suppressed as we no longer operate in the Rayleigh regime and we see the transmission dip decreasing.

A fit of the transmission dips was performed in order to extract system parameters and to investigate accordance between theory and experiment. In more detail, the system parameters were namely: the β factor, spontaneous emission rate γ, the rate of dephasing γ_d, the Fano parameter ξ, detuning from resonance f_0, the spectral diffusion σ_{sd} and the photon flux η. The results can be seen in the following table:

$\gamma(GHz)$	$\gamma_d(GHz)$	β	σ_{sd}	η	ξ
1.999 ± 0.008	0.05	0.9	0.56 ± 0.01	0.0572 ± 0.0005	0.131 ± 0.001

Note here that γ_d and β have no accompanied error values because they were fixed parameter during the fitting.

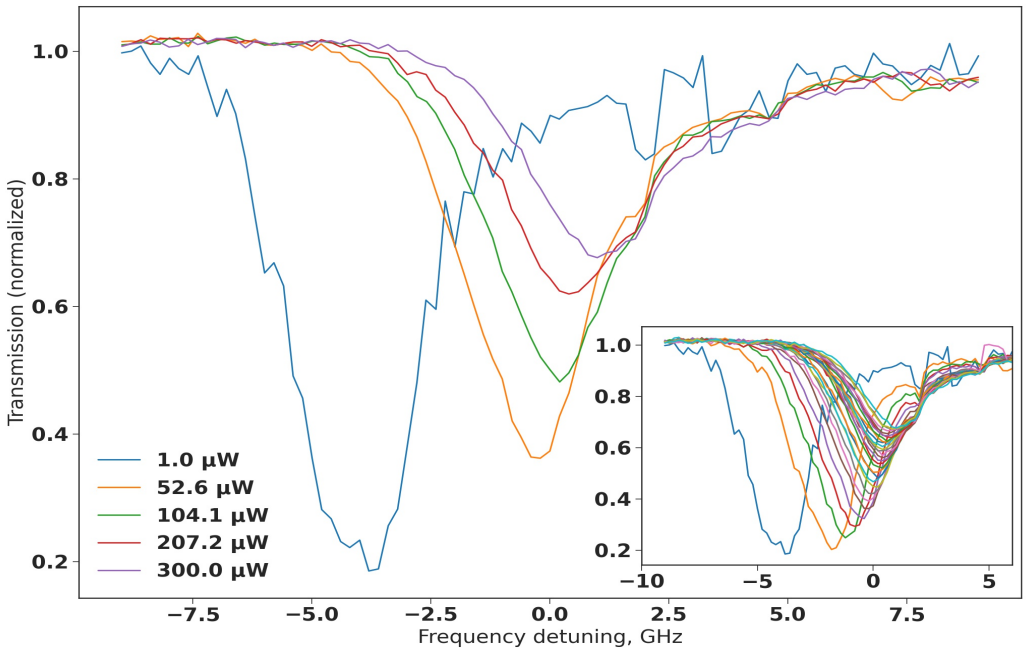

Figure 5.2: Transmission dips as a function of laser detuning for different values of excitation power. We observe that as the power increases, the resonant frequency and the width of the dip increases (power broadening), while the transmission dip decreases. In the inset all the recorded transmission dips are shown.

Some examples of the experimental data of the transmission curves with the fitted curves are shown in Figure 5.3.

The same measurements and subsequent analysis were performed for the reflected component. The acquired spectra can be viewed in Figure 5.4. Similarly to the transmission spectra, we notice the asymmetry of the curve, owed to the Fano resonance, the shift of the resonance frequency and the power broadening as the excitation power changes. Contrary to the transmission spectra, we observe that the peak increases, as the excitation power increases and the incoherent component is predominant.

5.1.2 Single photon nonlinearity

Finally, in order to show the saturation of the quantum dot, we plot the value of transmission at $\Delta = 0$ as a function of excitation power and mean photon number per lifetime (see Figure 5.5),

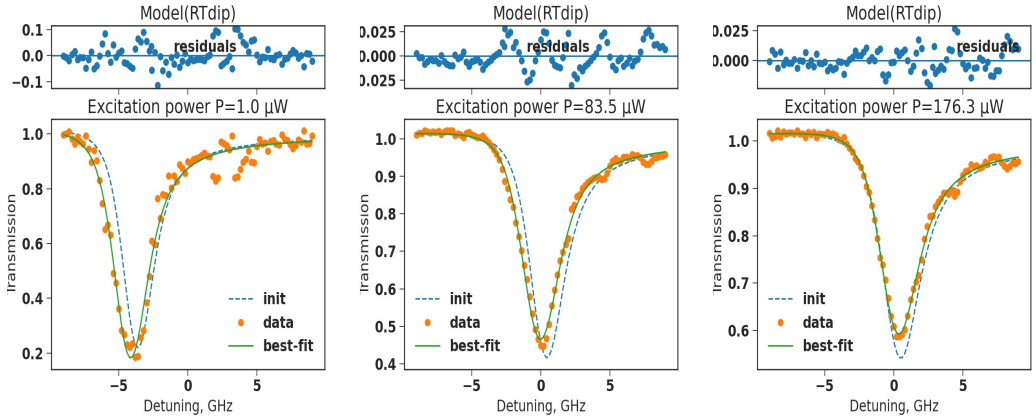

Figure 5.3: Transmission dips as a function of laser detuning for different values of excitation power with the fitted curves. The experimental data are shown as points, the initial fit as a dashed curve and the best fit as a solid curve.

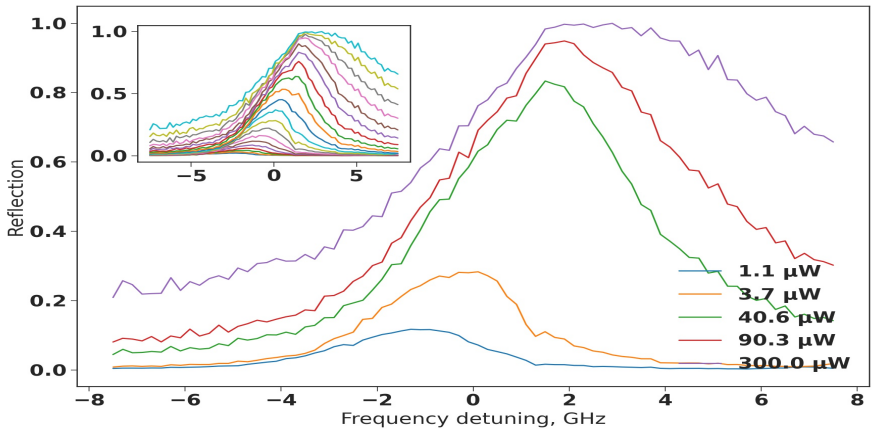

Figure 5.4: Reflection peaks as a function of laser frequency detuning for different values of excitation power. All of the acquired reflection spectra are shown in the inset.

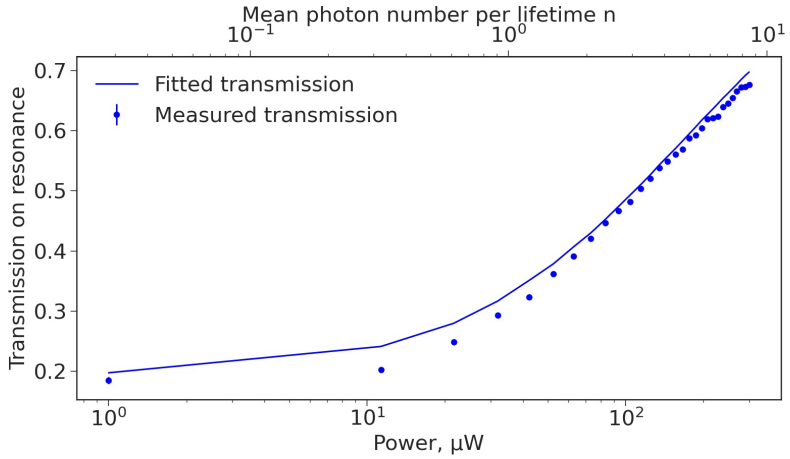

Figure 5.5: Saturation curve of the quantum dot. The dots represent the measured values of transmitted intensity on resonance and the solid line is the corresponding fit. On the lower horizontal axis the curve is plotted as a function of excitation power and on the upper as a function of the mean photon number per lifetime.

$$n = 2\frac{\Omega^2}{\Gamma^2} \tag{5.1}$$

where

$$\Omega^2 = \eta P \tag{5.2}$$

For the calculation of the Rabi frequency Ω the fitted values were used for the aforementioned parameters.

It can be seen from Figure 5.5 that when the excitation power is low, light doesn't go through the quantum dot but is mostly reflected, while for higher power the quantum dot is saturated. The fact that the transmission coefficient depends on the input power is referred to as a single photon non-linearity and it is a powerful result. Non-linearities usually occur at high intensities, but in the case of a quantum dot in a PCW driven by a resonant laser it is at the single photon level. Due to the single photon non-linearity the system has been referred to as "photon sorter", as it reflects single photons and transmits the higher order components, and can be used for deterministic Bell state analyzers and for operations such as gates [13].

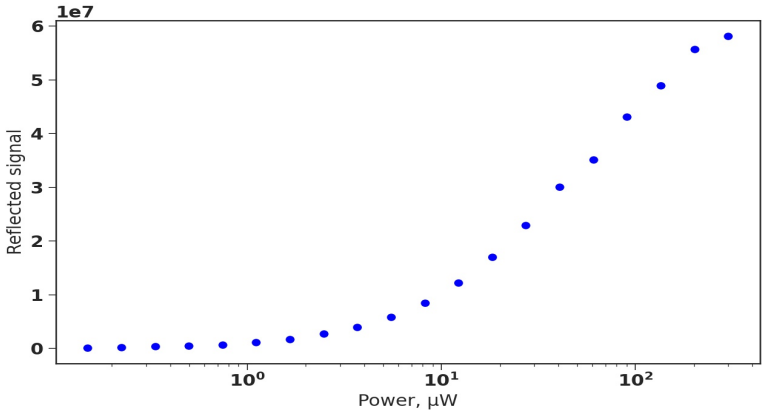

Figure 5.6: Saturation curve of the quantum dot using the reflection data. The dots represent the measured values of the reflected intensity on resonance. It should be noted here that the intensity of the reflected component was not normalized and as such, in high powers the reflection is due to spontaneous emission.

The saturation of the quantum dot can also be demonstrated by the reflection data. Similarly to the transmission, we plot the value of reflection on resonance, $\Delta = 0$ and we can see (Figure 5.6) that for higher powers the quantum dot is saturated. In this regime, most of the power is transmitted and the reflected component is almost exclusively comprised of spontaneously emitted photons.

5.2 Visibility as a function of excitation power

For this experiment, we excited the quantum dot by coupling the laser light into one of the gratings of the waveguide and collected light either by the same port (collection of the reflected light) or by the other port (collection of the transmitted light). The collected light was input into the unbalanced Mach-Zehnder type interferometer, described in Chapter 4, in order to measure the visibility of the light as the excitation power changes. According to the theory, we expect to see different behavior between the reflected and transmitted light as we change the power, due to the nonlinear interaction with the quantum dot.

5.2.1 Experimental setup and process

The experimental setup and process were identical, whether the visibility of interest was of the reflected or the transmitted light, with the only difference being the collection port.
The experimental setup consisted of the aforementioned interferometer and a quantum dot embedded in a one-dimensional photonic crystal waveguide placed in a cryostat to isolate the system from the environment and suppress decoherence mechanisms. The laser was a frequency tunable cw-laser that was split by a beamsplitter with a 90:10 ratio. The 10% fraction of the laser beam passed through a PID feedback loop for intensity stabilization. The intensity-stabilized beam was lead to excite the quantum dot and thus, the power that drove the quantum dot was adjustable by adjusting the voltage applied to the AOM. The 10% fraction of the laser beam was coupled into the "Laser" input of the interferometer and was used to stabilize its phase.
The whole measurement process was completely automated and run by a

computer program. The program firstly set the value of the excitation power. Various rounds of measurements were performed, with the power range being subject to minor changes, usually from $0.1\mu W$ to $300\mu W$. In contrast to the quantum dot saturation measurements, the laser frequency was locked at $f = 318.67GHz$ and in order to be resonant with the quantum dot at all driving powers, different values of voltage were applied to the quantum dot to slightly shift the energy transition, by use of the DC Stark effect, for every value of power. Thus, for each value of excitation power the voltage was scanned from 1.232V to 1.262V and for each value of voltage the number of counts was recorded in order to find the resonant value of voltage. The same measurement was then performed for a value of voltage that was off resonant at all powers. For each value of power and voltage (both on and off resonance), the linear polarizer was rotated by 180 degrees, effectively scanning the phase of the interferometer, in order to see interference fringes. Finally, the power was set at zero in order to measure the background counts.

5.2.2 Reflected light

To record interference fringes of the reflected light as a function of power, we changed the power from $P_{min} = 0.15\mu W$ to $P_{max} = 300\mu W$ and for each power, the linear polarizer was rotated by 360 degrees with a step of 7.5 degrees. The same procedure was conducted twice, one for voltage applied on the quantum dot to bring it on resonance with the laser and once for off resonant voltage.

The recorded counts can be seen in Figure 5.7. No pre-processing or data-cleaning was conducted as it was not necessary, with the sole exception of subtracting the measured background. We notice that the minimum value of the recorded counts was higher for the on resonant voltage in comparison to the off resonant, thus the quantum dot is effectively decreasing the visibility. In the case of the reflected signal, the off resonant counts should be equal to the background as the light shouldn't interact with the quantum dot and pass through the waveguide. The signal in this case is due to imperfections in the

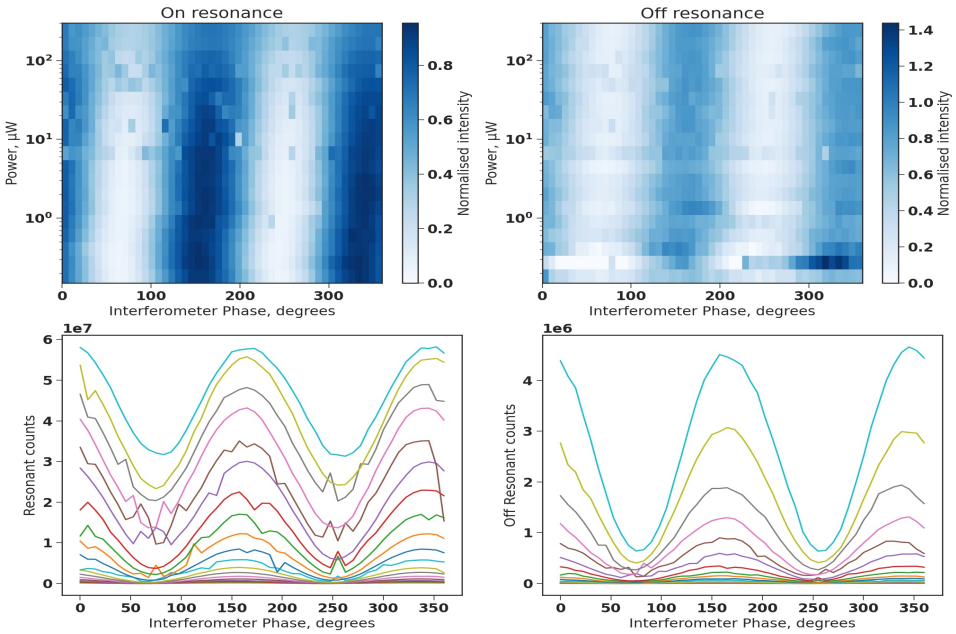

Figure 5.7: Top left: Intensity of light in the reflected mode for resonant voltage, as a function of interferometer phase and excitation power. The interference fringes are shown as blue-white stripes. We notice that as the power increases the fringes are smoothed out and the visibility decreases. Top right: Intensity of light in the reflected mode for non-resonant voltage, as a function of interferometer phase and excitation power. We note that the normalized intensity doesn't reach the maximum, but rather approximately half. In the case of the reflected light for non-resonant voltage no light should be reflected. Bottom left: Each interference curve corresponds to the interference of the light in the reflected mode for resonant voltage for each power as a function of interferometer phase. Bottom right: Each interference curve corresponds to the interference of the light in the reflected mode for non-resonant voltage for each power as a function of interferometer phase. When comparing the two bottom plots, we observe that when the light interacts with the quantum dot (left) the visibility decreases in comparison to when it doesn't (right). In addition, we notice that the maximum number of counts for the non-resonant plot is smaller than the on-resonant, as in this case we are measuring background.

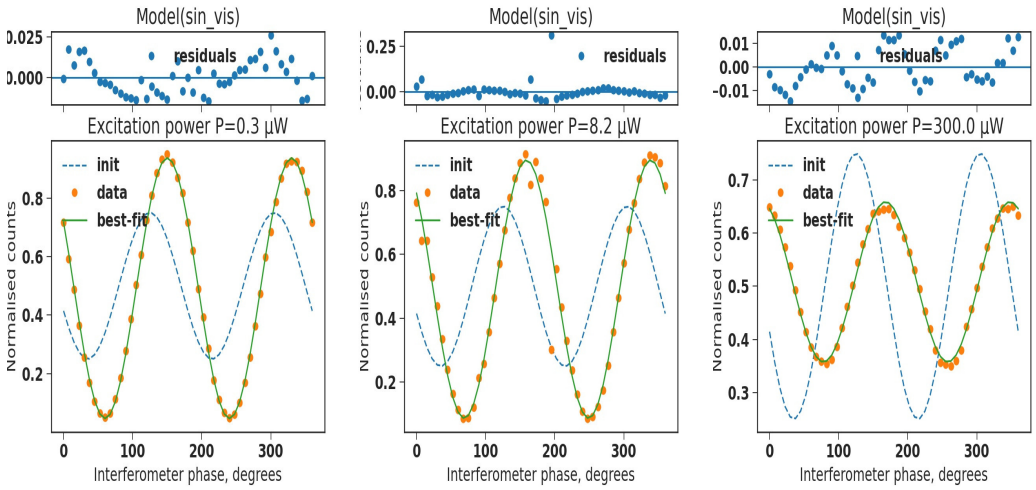

Figure 5.8: Interference fringes of the reflected light as a function of interferometer phase for three different values of excitation power. The experimental data are depicted as dots, the initial fit as a dashed line and the final fit as a solid line. The residuals of the fit are plotted as well.

way we collect the light and thus, the off resonant case shall not be further analysed for the reflected light.

A fit was performed on the recorded interference fringes in order to investigate how the visibility changes as a function of the driving laser power. Some examples can be seen in Figure 5.8.

It can be seen that the visibility drops as the excitation power increases. To further support that, we plot the value of the visibility as provided by the fit as a function of power (Figure 5.9). In the same figure, we also plot the visibility as calculated from the experimental data. Firstly, we see that the fit agrees quite well with the experimental data, however when it does not it tends to underestimate the visibility. We also notice that the error of the fitted visibility is larger in comparison to the estimated. The estimated visibility is derived by a very straightforward calculation and the error associated with it is given by the error propagation of the data. On the other hand, the fitted visibility for each power is the best fit of all the experimental points and is more sensitive to deviations from the expected sinusoidal behavior. However, the most important aspect of Figure 5.9 is the fact that the visibility decreases as the excitation power increases. When the power increases, the ratio of the coherent scattering and spontaneous emission decreases and as such the visibility decreases as well.

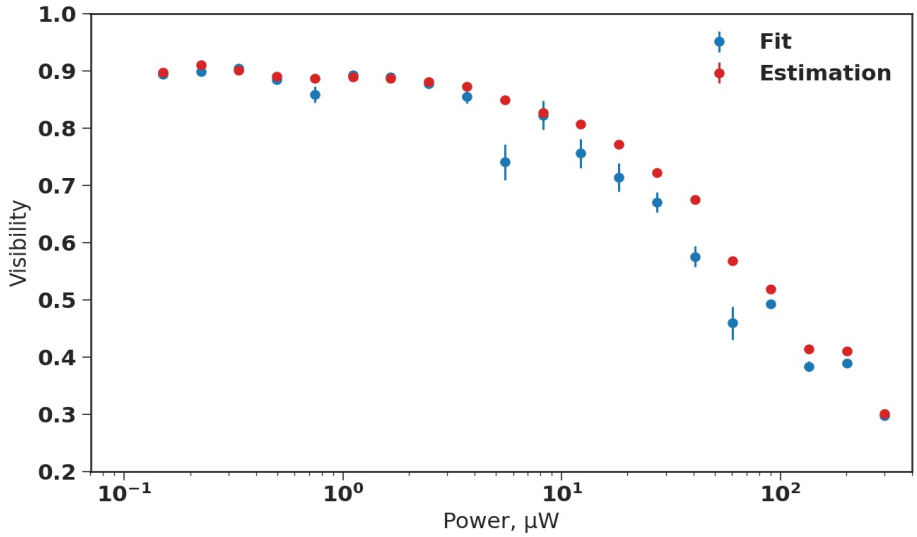

Figure 5.9: Fitted and estimated visibility as a function of laser power. As the coherent component takes over at high powers, the visibility drops.

5.2.3 Transmitted light

We follow the same procedure for acquiring and analyzing the data as in the previous section. The recorded interference fringes of the transmitted light, both for resonant and off resonant voltages are shown in Figure 5.11.

Similarly to the reflected light, we observe that the minimum value of intensity was higher for the resonant voltage than the off resonant, a signature of interaction with the quantum dot. In the case of transmission, the off resonant interference fringes characterize the performance of the interferometer and of the phase locking and therefore, shall be included in the analysis just as the resonant counts. The fit was performed here for both the on and off resonant counts and some examples can be viewed in Figures 5.11 and 5.12.

In the case of the off resonant counts, the visibility should be the same regardless of the excitation power, since the quantum dot is not interacting with the light field. To demonstrate this, we plot the off resonant visibility given by the fit and the visibility estimated by the experimental data, Figure 5.13 - plot on the right. We calculate the average value of visibility, both as fitted

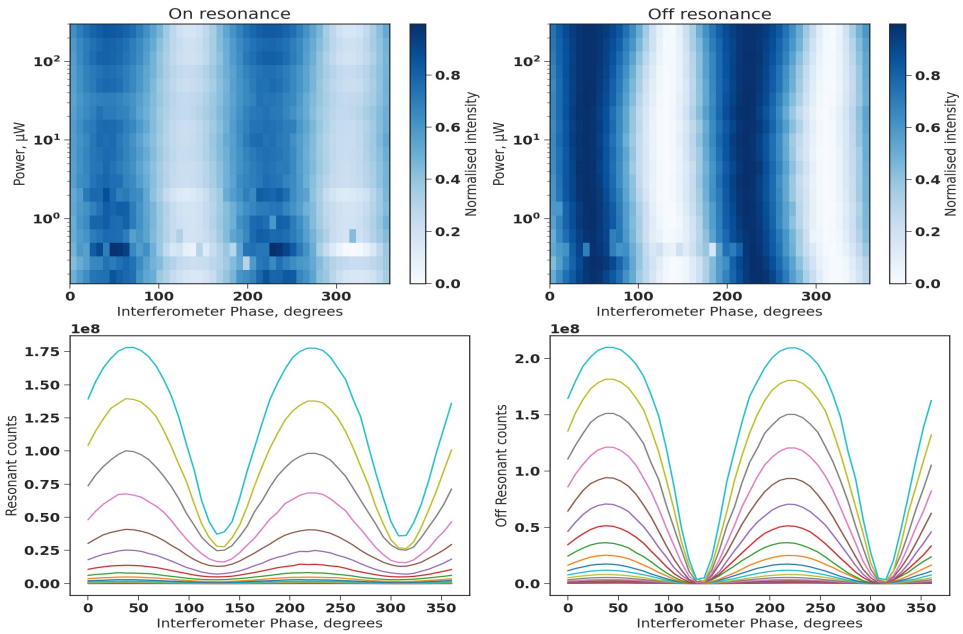

Figure 5.10: Top: Intensity of light in the transmitted mode for resonant voltage (plot on the left) and non-resonant voltage(plot on the right), as a function of interferometer phase and excitation power. The interference fringes are shown as blue-white stripes. We notice that at low powers the data are rather noisy and at larger powers the fringes become asymmetrical, due to the saturation of the photodetectors. Bottom: Each interference curve corresponds to the interference of the light in the transmitted mode for resonant (left plot) and non-resonant voltage (right plot) for each power as a function of interferometer phase. When comparing the two bottom plots, we observe that when the light interacts with the quantum dot (left) the visibility decreases in comparison to when it doesn't (right). The visibility of the fringes for the non-resonant voltage should not change as the power changes, as it characterizes the interferometer performance.

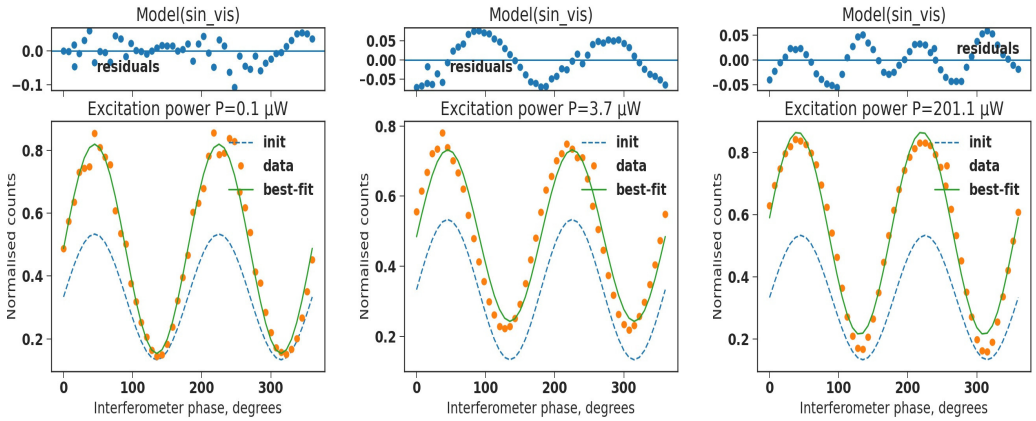

Figure 5.11: On resonant interference fringes of the transmitted light on resonance as a function of interferometer phase for three different values of excitation power. The experimental data are depicted as dots, the initial fit as a dashed line and the final fit as a solid line. The residuals of the fit are plotted as well.

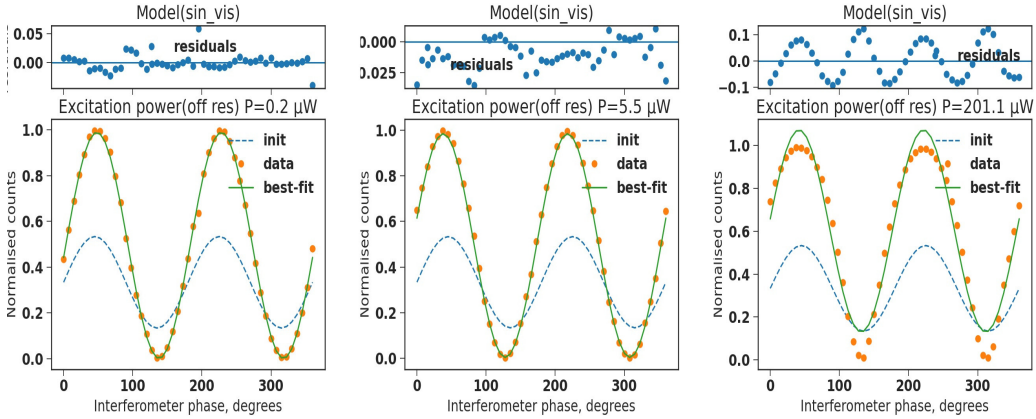

Figure 5.12: Off resonant interference fringes of the transmitted light on resonance as a function of interferometer phase for three different values of excitation power. The experimental data are depicted as dots, the initial fit as a dashed line and the final fit as a solid line. The residuals of the fit are plotted as well.

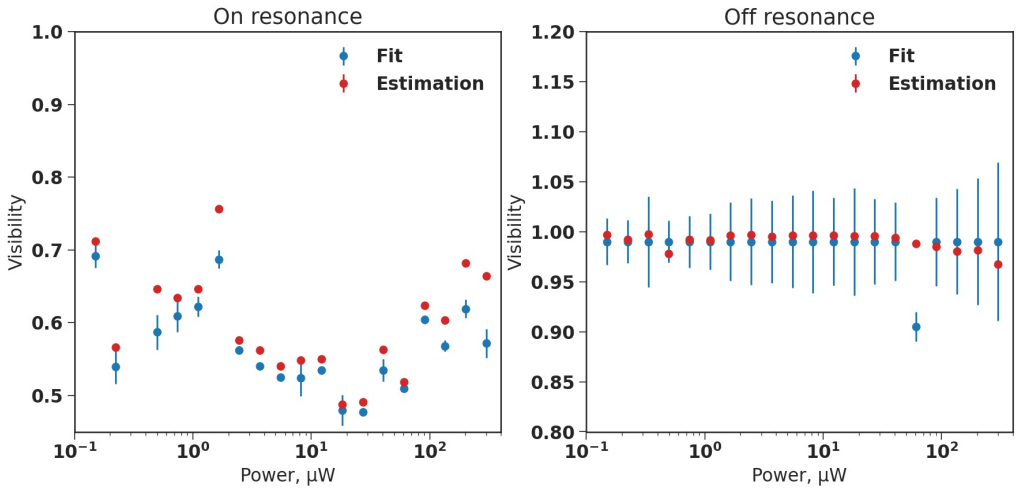

Figure 5.13: Fitted and estimated visibility as a function of driving power, both on and off resonant counts.

and estimated, to characterize the performance of the interferometer and the phase locking.

$$V_{fit} = 0.986 \pm 0.019$$
$$V_{est} = 0.991 \pm 0.008$$

Once more, we observe that the fit slightly underestimates the visibility and the errors associated with it are quite larger. A visibility of 99% means that the interferometer is stable and well-suited for applications where precision is essential.

We shall now move on to the more interesting case of the on resonant visibility. We observe that the visibility is rather high in the limit of very low power, where the coherent component of the transmission is dominant, i.e. photons are scattered by the TLS without interacting with it.

In the limit of very low excitation power, if the parameters characterizing the system were perfect then the transmission would be zero. The fact that there are dephasing mechanisms, messes up the coherences between the two states of the quantum dot and as a result the interference between the driving field and the scattered photons without absorption by the quantum dot - coherent component - is reduced. As such, there is a portion of the light field that passes

through the quantum dot, yielding non zero T that in the very low power limit is comprised of single photons. As the power is increased, the excited state population increases and thus the incoherent component starts to come into play in the form of emission. In this power region, the coherent and incoherent components interfere and produce squeezing in the two-photon state which is produced by the destructive interference of the driving field with the scattered photons and the visibility is decreased. At higher powers, what we see is mostly the signal that doesn't interact with the quantum dot and spontaneous emission.

5.3 Time-energy entanglement

The objective for this series of measurements was to record the interference pattern of the two-photon 2nd-order coherence function using a Franson interferometer, i.e. two identical UMZIs, one with constant phase and another with a variable phase. Thus, the transmitted light from the cryostat was split in half and each half was guided into the one of the unbalanced interferometers. At each of the interferometers, the photon can either propagate through the short or the long path and then we measure the coincidence count rate. The interference in the coincidence counts arises from the fact that the emitted photons are energy and time correlated. More specifically, the emitted photons have a time uncertainty τ, inherited by the natural linewidth of the quantum dot. Conversely, the energy uncertainty of each individual photon is much larger than the uncertainty in the total energy $\omega_1 + \omega_2$ which allows us to write equation 3.41 and derive the coincidence count rate 3.42 as a function of interferometer phase.

5.3.1 Phase scan experimental process

In order to measure the visibility and demonstrate the entangled state, by using Equation 3.37, we performed interferometer phase scans and recorded histograms at each of the two detectors (note here that only one of the two detectors of each interferometer were used). The scans were repeated for three different values of power, namely $P = 2.5, 5, 15\mu W$, however the power was kept constant for the duration of each scan. The frequency of the laser was also kept constant, $f = 318.67GHz$ and thus, we scanned the voltage to be resonant with the quantum dot. The interferometer phase scan was from $0°$ to $180°$ with a step of $12°$. We define four CHSH angles for the first interferometer, $0°, 45°, 90°, 135°$ and four more for the second, $+22.5°$ from the first one such that the bases of the two interferometers are at $45°$ with each other. The aforementioned angles are often termed as the *Bell angles* and they yield the maximum violation of Bell and CHSH inequalities. However, in practise those angles have to be corrected and therefore the first step of measurement process was to calibrate the UMZIs to find the Bell angles of our experiment. After finding them, we rotate the interferometers such that they are at those angles. Once again, the whole measurement process was completely automated. We perform voltage scan to find the resonant voltage and afterwards we apply it on the quantum dot. Finally, while maintaining one of the interferometers at a constant phase, we scan the phase of the other and record histograms in each detector in order to compute the coincidence count rate and consequently the 2nd-order coherence function of the two-photon state.

5.3.2 2nd-order coherence function

From the recorded histograms, we sum the measured count rates to retrieve the coincidence count rate and we plot it as a function of delay τ, ns. Afterwards, we divide by the average coincidence count rate and thus we normalize $g^{(2)}$.

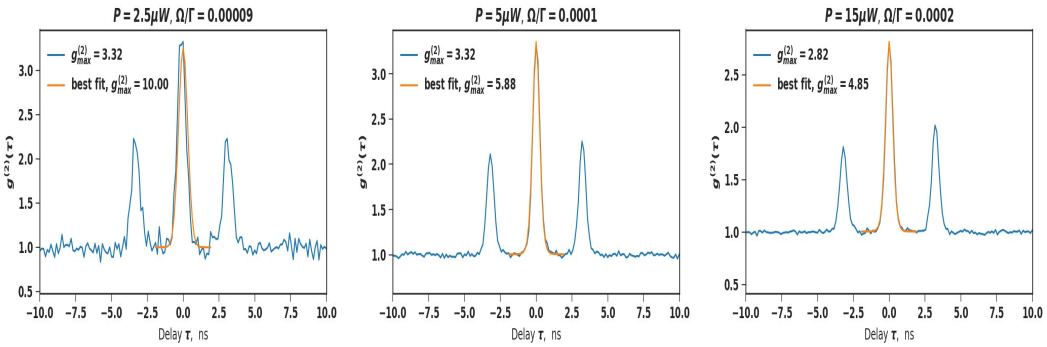

Figure 5.14: 2nd-order coherence function $g^{(2)}$ as a function of delay time τ for three different excitation powers. We can distinguish three different peaks, corresponding to the three possible states in the interferometers. The blue curve represents the experimental data while the orange peak represents the theoretical fit performed convoluted with the detector's IRF. The maximum value of $g^{(2)}$ is written as calculated by the data and as fitted in the case of an ideal detector.

Three different peaks emerge, corresponding to the three possible outcomes. The central peak corresponds to the case of both the photons choosing the same path, either short or long, in their respective interferometers while the side peaks show the interference of the photons propagating in different paths. The height and width of the peaks is modified by the detector's internal response function. In the ideal case, the IRF should be a δ function, however in reality it is described by a Gaussian distribution with parameters given by the specifications of the exact model of the detector. The effect of the non-perfect detection is to broaden the peaks and underestimate the maximum value at zero delay. We perform a theoretical fit of a double exponential decay and we convolute it with the Gaussian IRF. The data and fits can be viewed in Figure 5.14.

5.3.3 Visibility of coincidences

We proceed to measure the interference pattern of the coincidence peaks as we change the phase of one of the UMZIs, while keeping the other one stable. We perform this three times, one for each of the excitation powers mentioned in the previous section and for each power we scan the phase four times, one

for each of the CHSH angles of the stable interferometer. For every one of the measurements, the background counts were measured and subtracted from the peaks. We are interested in the behavior of the central peak, as it is the one that shows the interference and consequently, will determine if the state is entangled and if it violates locality.

The interference pattern of the central peak as we scan the phase of the interferometer for all powers can be seen in Figure 5.15. The experimental data are shown as dots and the theoretical fit that was performed is shown with solid lines. The three different plots correspond to three different excitation powers and for each of them, the interference pattern has been plotted for each of the CHSH angles determined by the initial calibration for the second (stable) interferometer. We observe that in the case of $P = 2.5\mu W$, the data are quite noisy as we are close to the detector's dark count rate. In addition, we can see from the plots that the visibility of the coincidences reduces as the driving power increases, same as for the transmitted and reflected light.

Finally, we determine if the state is entangled and if it violates locality. The theoretical fit of the coincidences provided for each power, 4 fitted values of the visibility and a corresponding uncertainty, one for each of the CHSH angles. Using Equation 3.37 we estimate the S parameter for each of the fitted parameters of visibility and the error is calculated according to the error propagation. The average values are the mean of the four fitted and the error represents their standard deviation.

Excitation power $P = 2.5\mu W$

	$\phi 2 = 146°$	$\phi 2 = 191°$	$\phi 2 = 236°$	$\phi 2 = 281°$	Average
V_{fit}	0.93 ± 0.06	0.99 ± 0.15	0.82 ± 0.14	0.91 ± 0.13	0.91 ± 0.07
S	2.63 ± 0.17	2.80 ± 0.43	2.32 ± 0.41	2.58 ± 0.38	2.58 ± 0.20

The visibility of the coincidence counts of the central peak for the low power of $P = 2.5\mu W$ is quite large, almost unity for $\phi_2 = 191°$ and consequently, the S parameter of the CHSH is estimated to be close to its maximum value, $S_{max} = 2\sqrt{2}$. However, as was also shown in Figure 5.14, for such a low value of power the data are quite noisy and due to that we have quite large error in the fitted visibility and the S parameter. Even though the errors are larger

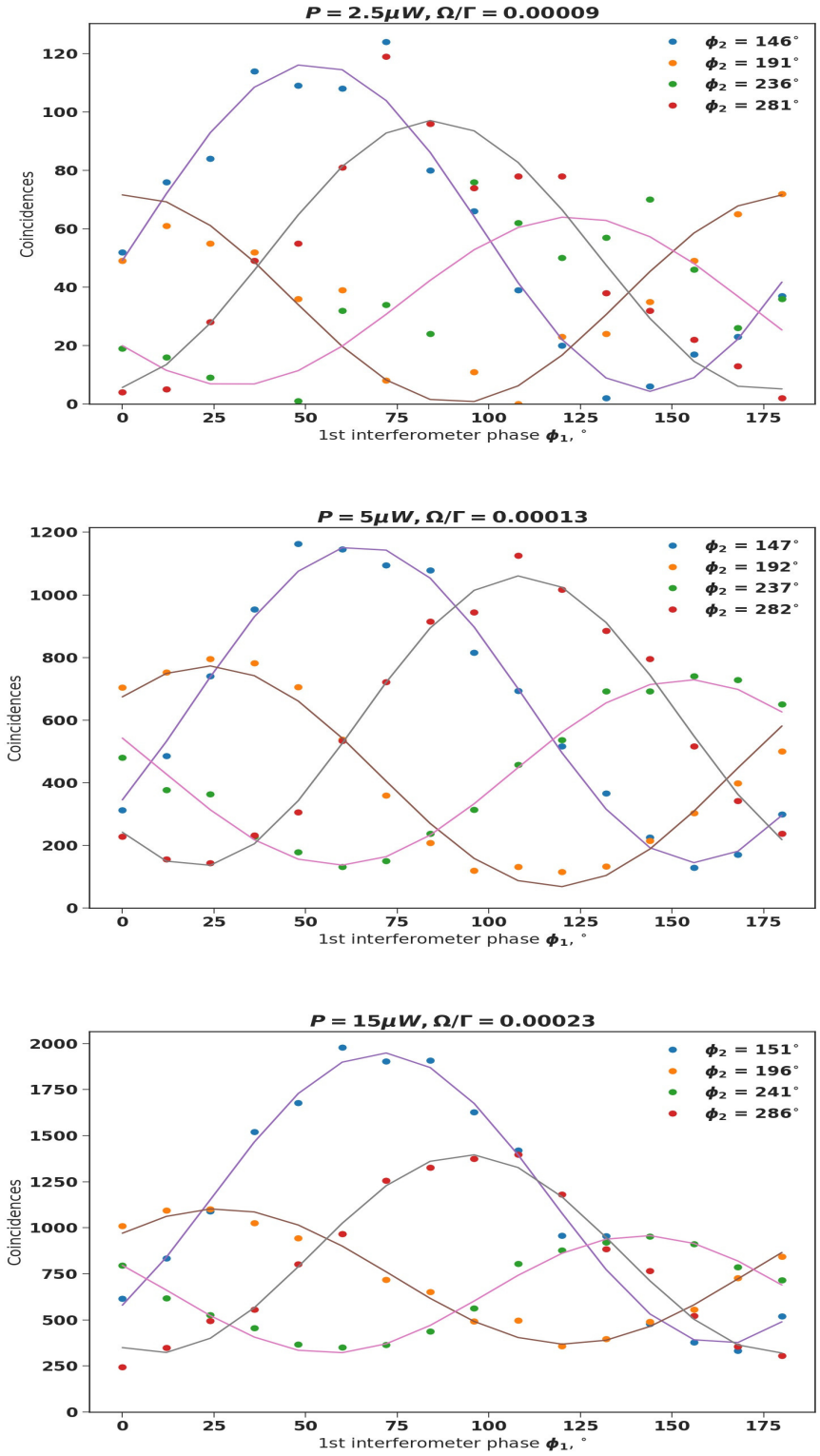

Figure 5.15: Coincidence count rate as a function of intereferometer phase. The experimental data are depicted as dots and the solid curves show the corresponding fits. We can see the interference fringes for three chosen excitation powers and for the four CHSH angles, chosen by the initial calibration of the interferometers.

than ideal, the visibility is significantly above the $1/\sqrt{2}$ threshold for entangled state. The S parameter is significant as well, meaning that the post-selected two-photon state in the transmitted mode is not only time-energy entangled, but doesn't obey locality.

Excitation power $P = 5\mu W$

	$\phi 2 = 147°$	$\phi 2 = 192°$	$\phi 2 = 237°$	$\phi 2 = 282°$	Average
V_{fit}	0.78 ± 0.03	0.84 ± 0.05	0.68 ± 0.03	0.78 ± 0.03	0.77 ± 0.07
S	2.20 ± 0.08	2.37 ± 0.14	1.93 ± 0.09	2.20 ± 0.07	2.17 ± 0.18

When increasing the power to $P = 5\mu W$, the visibility slightly drops and as a consequence, the S parameter drops as well. In this case, we can claim that the two-photon state is entangled, however the error of the S parameter is quite large and as such we cannot claim violation of local hidden variables.

Excitation power $P = 15\mu W$

	$\phi 2 = 151°$	$\phi 2 = 196°$	$\phi 2 = 241°$	$\phi 2 = 286°$	Average
V_{fit}	0.68 ± 0.03	0.50 ± 0.03	0.500 ± 0.004	0.65 ± 0.03	0.58 ± 0.09
S	1.93 ± 0.08	1.41 ± 0.07	1.41 ± 0.01	1.84 ± 0.09	1.65 ± 0.28

Finally, when increasing the driving power to $P = 15\mu W$ we see that the visibility is significantly reduced. We can still claim that the state is entangled, however in this driving power regime the state obeys local realism.

In the following plots, we can see the interference fringes of the measurement of the side peaks, in order to demonstrate the difference between them and the central peak. It can be seen that the intensity in this case stays mostly constant, yielding visibilities around $10\% - 30\%$.

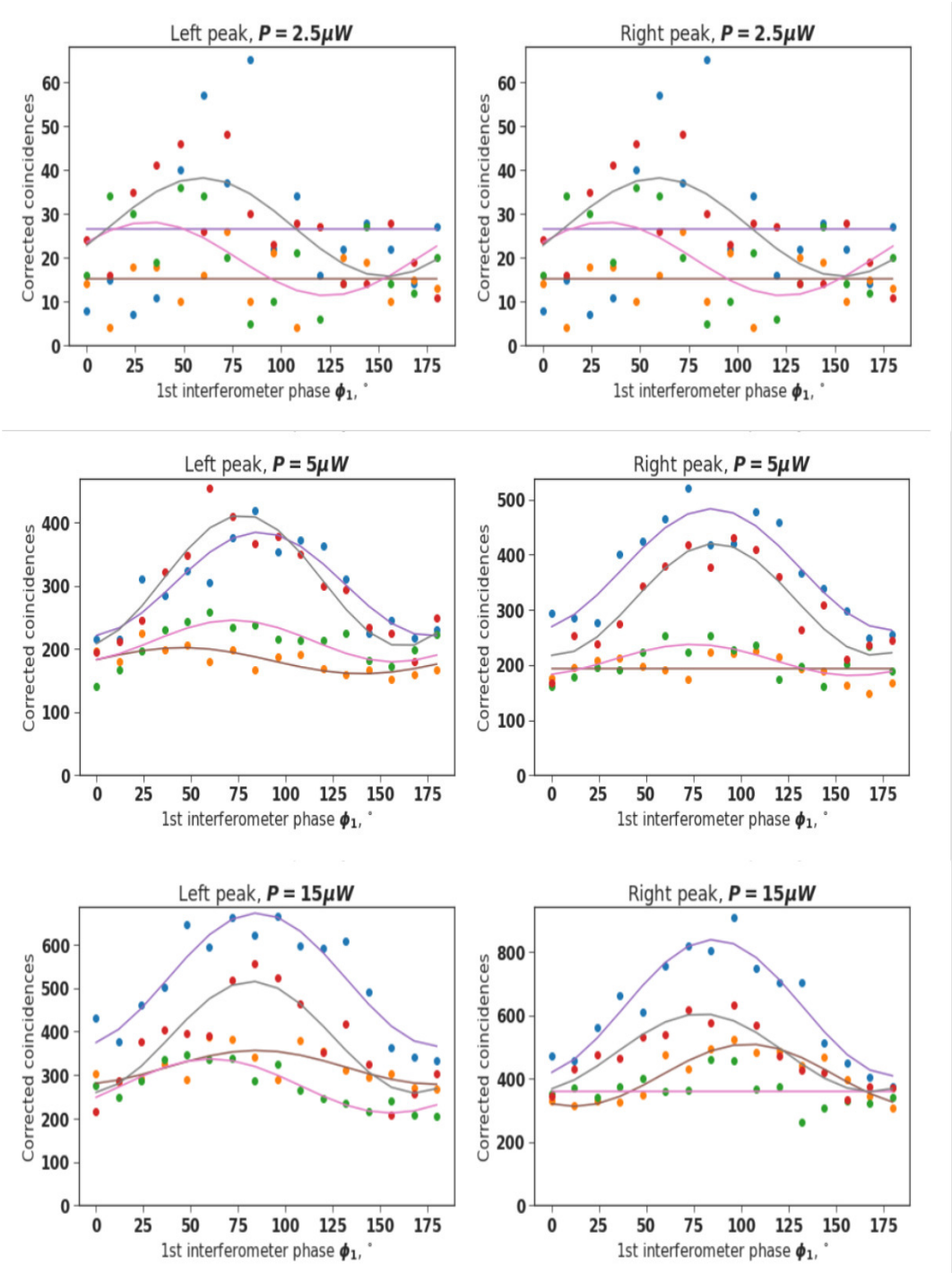

Figure 5.16: Coincidence count rate of the side peaks as a function of intereferometer phase. The experimental data are depicted as dots and the solid curves show the corresponding fits. We can see the interference fringes for three chosen excitation powers and for the four CHSH angles, chosen by the initial calibration of the interferometers.

6 Conclusions and Future work

6.1 Summary

For this thesis, the properties of a light field that interacted with a solid-state emitter embedded in a waveguide were investigated and in the process an unbalanced Mach-Zehnder interferometer was constructed. The UMZI was made in order to measure the visibility of the light in the transmitted and reflected modes of the waveguide, as well as the visibility of the coincidences of the two-photon component of the transmitted mode. It can also be used for the control of the relative phase between laser pulses that we can use to excite the quantum dot. The UMZI introduces a set delay corresponding to its 1m path length difference and a variable phase that is set by polarization elements. The variable phase can be controlled precisely and automatically via PC programs that can be integrated in coding languages. We ensure the interferometer's stability by the *lock-in amplifier* technique, inserting a control signal into a PID feedback circuit controlled by a microcontroller. The visibility for a laser beam is above 99%, meaning that the UMZI is stable and the locking is efficient and consequently, it can be used for applications where precision is sought. Having in our possesion the UMZI, we measured the visibility of the driving light and of the coincidence rate, where we made use of another preexisting identical UMZI to realize the Franson interferometer.

6.2 Emitter saturation

The first experiment that was conducted aimed to demonstrate the saturation of the emitter at high powers. To that end, we excited the quantum dot by coupling the light field into one of the waveguide's gratings and then measured the intensity of the light of the transmitted and reflected mode as a function of detuning. By plotting the value of transmission on resonance we demonstrated the saturation of the quantum emitter at high powers and the single-photon nonlinearity in low powers, where the laser beam can be approximated by a weak coherent state. In this regime, termed as the *Rayleigh regime*, the quantum dot effectively reflects the single photon component of the weak coherent beam and transmits the two photon component due to the interference between the scattered photons and the emitted field.

6.3 Visibility of transmission and reflection

We probed the aforementioned interference between the coherent and incoherent component by collecting the reflected or the transmitted light and inserting it into the UMZI in order to measure the visibility as a function of the laser driving power. We notice that both for the reflected and for the transmitted fields, the visibility drops when the light is resonant with the quantum dot, evidence of the TLS-light interaction, when compared to the non-resonant voltage. Also similar in both cases is that even though the theoretical fit mostly agrees with the data, when it deviates, it tends to underestimate the visibility and produce large errors for the fitted parameters. This could be a sign of noisy data that could be fixed while simply gathering more statistics or by implementing a bit of data-cleaning.

A significant difference between the reflected and transmitted fields is the trend the visibility follows as a function of laser power. In the reflected field case, the visibility is reduced as the power is increased, while the transmitted field's visibility drops to a minimum but then rises again for high powers. In very low powers, the coherent component of the field is dominant while all

the population is in the ground state. In this case, the incident field should be reflected if there are no dephasing mechanisms. Because of the existence of pure dephasing, some fraction of the incident field manages to pass through the emitter without interacting with it and this is the reason we see high visibility in the transmitted mode. As the power increases, the excited state starts to become populated and thus to emit photons. The emitted photons, *incoherent component*, interact with the scattered photons, *coherent component*, and we see a drop in the visibility which presumably would approach zero if not for pure dephasing. In this power region, the incident two-photon states are scattered inelastically by the quantum dot and the emitted photons are time-energy correlated with a smaller time uncertainty that the incoming, *squeezing in the transmitted mode*. In high powers, the quantum dot starts to become saturated and the light field just passes through without interaction, which is why we see the visibility rise.

Regarding the reflected component, for very low powers we see a high value of visibility, that again would be higher if not for pure dephasing, as most of the light field is reflected due to destructive interference with the coherent component. As the power rises, the coherent/incoherent component reduces and so does the visibility until it drops to zero.

Finally, for the case of the non-resonant phase scans, the transmitted field in this case is just a coherent laser beam that hasn't interacted with the emitter and thus its visibility characterizes the performance and stability of the interferometer and the phase locking. The reflected field for non-resonant voltage, should be equal to the background and it is a measure of imperfections in our collection scheme.

6.4 Time-energy entanglement

Lastly, for the final experiment of this thesis, we used two identical UMZIs to measure the visibility of the coincidence count rate of the post-selected two-photon state in the transmitted mode. A visibility larger than $1/\sqrt{2}$ proves entanglement in the two-photon state. The visibility is connected to the

S parameter of the CHSH inequality by Equation 3.37 and if $S > 2$ then we can claim that the two-photon state doesn't obey locality. For all of our measurements, we found that the two-photon state was indeed entangled due to time-energy correlations inherited by the scattering by the emitter. We also found that $S > 2$ in the case of $P = 2.5\mu W$, indicating that the state doesn't obey local realism. However for $P = 5\mu W$ the error was too large to claim nonlocality and for $P = 15\mu W$ we found $S < 2$. The difference in driving power is not large enough to explain this shift, however many assumptions were made to derive the aforementioned numbers. For example, in the theoretical model describing the correlation between the photons of the two-photon state, pure dephasing, spectral diffusion were not included or the influence of a non-unity β factor were not included. Another potential reason for this, could be that the detector's response is not ideal and it influences the photon statistics of the incident light. A more careful study of the detector's IRF would be a beneficial first step towards improving the reliability of the CHSH phase scans.

7 Bibliography

[1] Marta Arcari, Immo Söllner, Alisa Javadi, S Lindskov Hansen, Sahand Mahmoodian, Jin Liu, Henri Thyrrestrup, Eun Hye Lee, Jin Dong Song, Søren Stobbe, *et al.* „Near-unity coupling efficiency of a quantum emitter to a photonic crystal waveguide“. In: *Physical review letters* 113.9 (2014), p. 093603.

[2] Paola Borri, Wolfgang Langbein, Stephan Schneider, Ulrike Woggon, Roman L Sellin, Dongxun Ouyang, and Dieter Bimberg. „Ultralong dephasing time in InGaAs quantum dots“. In: *Physical Review Letters* 87.15 (2001), p. 157401.

[3] Alistair J Brash, Jake Iles-Smith, Catherine L Phillips, Dara PS McCutcheon, John O'Hara, Edmund Clarke, Benjamin Royall, Luke R Wilson, Jesper Mørk, Maurice S Skolnick, *et al.* „Light scattering from solid-state quantum emitters: beyond the atomic picture“. In: *Physical Review Letters* 123.16 (2019), p. 167403.

[4] John F Clauser, Michael A Horne, Abner Shimony, and Richard A Holt. „Proposed experiment to test local hidden-variable theories“. In: *Physical review letters* 23.15 (1969), p. 880.

[5] James D Franson. „Bell inequality for position and time“. In: *Physical review letters* 62.19 (1989), p. 2205.

[6] Knight Gerry. *Introductory Quantum Optics*. Cambridge University press, 2004.

[7] Dominic Hallett, Andrew P Foster, David L Hurst, Ben Royall, Pieter Kok, Edmund Clarke, Igor E Itskevich, A Mark Fox, Maurice S Skolnick, and Luke R Wilson. „Electrical control of nonlinear quantum optics in a nano-photonic waveguide“. In: *Optica* 5.5 (2018), pp. 644–650.

[8] Lukas Hanschke, Lucas Schweickert, Juan Camilo López Carreño, Eva Schöll, Katharina D Zeuner, Thomas Lettner, Eduardo Zubizarreta Casalengua, Marcus Reindl, Saimon Filipe Covre da Silva, Rinaldo Trotta, *et al.* „Origin of Antibunching in Resonance Fluorescence“. In: *Physical Review Letters* 125.17 (2020), p. 170402.

[9] Alisa Javadi, I Söllner, Marta Arcari, S Lindskov Hansen, Leonardo Midolo, Sahand Mahmoodian, G Kiršanskė, Tommaso Pregnolato, EH Lee, JD Song, *et al.* „Single-photon non-linear optics with a quantum dot in a waveguide“. In: *Nature communications* 6.1 (2015), pp. 1–5.

[10] H Jeff Kimble. „The quantum internet“. In: *Nature* 453.7198 (2008), pp. 1023–1030.

[11] Şükrü Ekin Kocabaş, Eden Rephaeli, and Shanhui Fan. „Resonance fluorescence in a waveguide geometry“. In: *Physical Review A* 85.2 (2012), p. 023817.

[12] Midolo L. *Advanced quantum optics and quantum photonics, Lecture notes*. 2021.

[13] Hanna Le Jeannic, Tomás Ramos, Signe F Simonsen, Tommaso Pregnolato, Zhe Liu, Rüdiger Schott, Andreas D Wieck, Arne Ludwig, Nir Rotenberg, Juan José García-Ripoll, *et al.* „Experimental reconstruction of the few-photon nonlinear scattering matrix from a single quantum dot in a nanophotonic waveguide“. In: *Physical Review Letters* 126.2 (2021), p. 023603.

[14] Marcelo Alejandro Luda, Martin Drechsler, Christian Tomás Schmiegelow, and Jorge Codnia. „Compact embedded device for lock-in measurements and experiment active control“. In: *Review of Scientific Instruments* 90.2 (2019), p. 023106.

[15] Ivan Marcikic, Hugues De Riedmatten, Wolfgang Tittel, Hugo Zbinden, Matthieu Legré, and Nicolas Gisin. „Distribution of time-bin entangled qubits over 50 km of optical fiber“. In: *Physical Review Letters* 93.18 (2004), p. 180502.

[16] Jeremy L O'brien, Akira Furusawa, and Jelena Vučković. „Photonic quantum technologies“. In: *Nature Photonics* 3.12 (2009), pp. 687–695.

[17] Catherine L Phillips, Alistair J Brash, Dara PS McCutcheon, Jake Iles-Smith, Edmund Clarke, Benjamin Royall, Maurice S Skolnick, A Mark Fox, and Ahsan Nazir. „Photon statistics of filtered resonance fluorescence“. In: *Physical Review Letters* 125.4 (2020), p. 043603.

[18] Roman Schnabel, Nergis Mavalvala, David E McClelland, and Ping K Lam. „Quantum metrology for gravitational wave astronomy“. In: *Nature communications* 1.1 (2010), pp. 1–10.

[19] Carsten HH Schulte, Jack Hansom, Alex E Jones, Clemens Matthiesen, Claire Le Gall, and Mete Atatüre. „Quadrature squeezed photons from a two-level system“. In: *Nature* 525.7568 (2015), pp. 222–225.

[20] Pascale Senellart, Glenn Solomon, and Andrew White. „High-performance semiconductor quantum-dot single-photon sources“. In: *Nature nanotechnology* 12.11 (2017), pp. 1026–1039.

[21] Signe Folden Simonsen. *Master Thesis: Understanding nonlinearities in a photonic crystal waveguide with a quantum dot*. 2019.

[22] Petru Tighineanu, Chris L Dreeßen, Christian Flindt, Peter Lodahl, and Anders S Sørensen. „Phonon decoherence of quantum dots in photonic structures: Broadening of the zero-phonon line and the role of dimensionality“. In: *Physical Review Letters* 120.25 (2018), p. 257401.

[23] Rahul Trivedi, Kevin A Fischer, Jelena Vučković, and Kai Müller. „Generation of Non-Classical Light Using Semiconductor Quantum Dots“. In: *Advanced Quantum Technologies* 3.1 (2020), p. 1900007.

[24] Florian Wolfgramm, Chiara Vitelli, Federica A Beduini, Nicolas Godbout, and Morgan W Mitchell. „Entanglement-enhanced probing of a delicate material system“. In: *Nature Photonics* 7.1 (2013), pp. 28–32.